# LUND UNIVERSITY
## Faculty of Science

Template-assisted Electrodeposition and
Model Electrodes Studied by Electron Microscopy
and High Energy X-ray Diffraction

Hanna Sjö

Thesis submitted for the degree of Master of Science
Project duration: 9 months

# Abstract

There is a great interest in studying detailed changes at electrode surfaces during electrochemical processes to better understand the electrochemical reactions at the electrode surface-liquid interface and improve the electrode efficiency. The Au(110) surface has a known (1×2) missing row reconstruction in vacuum conditions, which can change into higher-order (1×3), (1×5), and (1×7) depending on environment. Although less studied than under vacuum conditions, surface studies have been performed during electrochemical reactions where similar reconstructions have been noted. In this thesis high energy surface x-ray diffraction measurements from a Au(110) surface in $HClO_4$ and $H_2SO_4$ have been performed at varying potentials both *in situ* and *ex situ*. The results confirm previously shown electrode potential-dependence of the reconstruction in $HClO_4$. A (1×3) missing row reconstruction is present at negative potentials, which transitions into a (1×2) reconstruction before the recondition is effectively lifted at higher positive potentials. The transitions are shown to still contain (1×3) reconstruction up until a clear (1×2) reconstruction is present, which can indicate domains of (1×3) and (1×2) reconstruction coexisting. For Au(110) in $H_2SO_4$, there is a similar transition behavior from a (1×3) reconstruction. The transition seems to occur at higher potentials than for $HClO_4$, but a clear (1×2) reconstruction is never present.

A second project focused on the synthesis process of nanoporous templates and electrodeposition of Sn and Pt. A two-step anodization process was used to create porous alumina templates with well-ordered pores. Electrodeposition is a method by which the nanowires can be built atom by atom in the pores without limitations of sample size. The deposition and wire properties have been studied before. However, there is an interest in developing the deposition process and studying the efficiency to enable the fabrication of bi-metallic SnPt nanowires. Sn electrodeposition was performed with a Sine potential, a symmetrical pulse shape, and an asymmetrical pulse shape. While the pulsed deposition resulted in materials in the pores, the efficiency was low, and the pores were not filled even after long deposition times. The asymmetrical pulse shape enabled higher pore filling. The Pt deposition with the same methods was unsuccessful due to high solution acidity. Nonetheless, the new pulse shape opens up for further development of the deposition process.

# Contents

# 1 Abbreviations

| | |
|---|---|
| **AC** | Alternating Current |
| **CE** | Counter Electrode |
| **CTR** | Crystal Truncation Rod |
| **CV** | Cyclic Voltammetry |
| **DC** | Direct Current |
| **FCC** | Face-Centered Cubic |
| **FIB** | Focused Ion Beam |
| **HESXRD** | High Energy Surface X-Ray Diffraction |
| **LINAC** | Linear Accelerator |
| **NPA** | Nano-porous Alumina |
| **PAA** | Porous Anodic Alumina |
| **PE** | Primary Electrons |
| **PED** | Pulsed Electrodeposition |
| **SAXS** | Small Angle X-Ray Scattering |
| **SE** | Secondary Electrons |
| **SEM** | Scanning Electron Microscope |
| **SOR** | Surface Optical Reflectance |
| **SXRD** | Surface X-Ray Diffraction |
| **UHV** | Ultrahigh Vacuum |
| **WAXS** | Wide Angle X-Ray Scattering |
| **WE** | Working Electrode |
| **XRD** | X-Ray Diffraction |

# 2  Introduction

Electrochemistry is a field at the boundary between chemistry and electricity where chemical reactions are driven by the exchange of electrons. The reactions in electrochemistry are divided into oxidation and reduction reactions depending on if the material loses or gains one or more electrons. The basic description of an electrochemical reaction is

$$\text{Red} \xrightleftharpoons[\text{reduction}]{\text{oxidation}} \text{Ox} + ne^-, \tag{1}$$
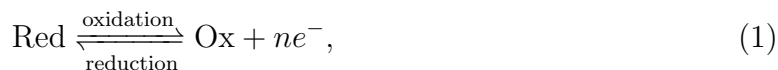
where Red is the reducing agent, Ox is the oxidation agent, and $n$ is an integer indicating the number of electrons in the reaction. The reactions can be spontaneous if the reaction is energetically favorable, but since they are dependent on the exchange of electrical energy, they can also be controllable by current. The possibility to drive reactions and store electrons make electrochemical reactions vital in the development of modern fuel and energy devices. To understand the electrochemical reactions, there is a need to describe the basic electrochemical system. The system is often referred to as an electrochemical cell, where the base is one or more electrodes connected to a power supply. An electrode is referred to as an anode or cathode depending on whether oxidation or reduction occurs. The basic electrochemical set-up can be seen in Figure 1. It generally contains a working electrode (WE), counter electrode (CE), and reference electrode. The electrodes are placed in an electrolyte that is a solution with ions. A potential over the WE and CE will attract the ions to the electrodes with the opposite charge. Depending on the current direction, a reduction or oxidation of ions will occur at the CE surface and vice versa at the WE. The reference electrode is used to make potential measurements possible, but if there is no need to measure the potential carefully, a two-electrode system can be used without a reference electrode. The reference electrodes needs to be stable and have a well-known electrode potential. This is often achieved by having a redox system with a saturated solution as the electrode. In the set-up in Figure 1, the reference electrode is used as an half-cell which can give information about the potential over the other electrodes[1].
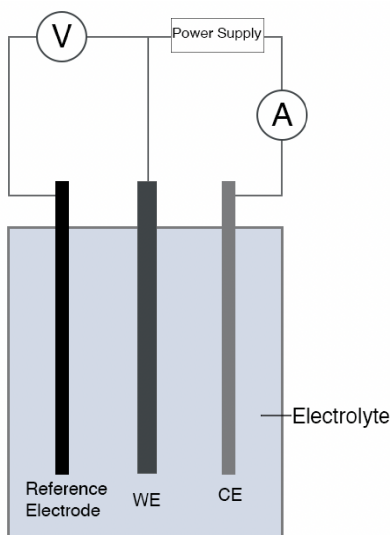


**Figure** 1: The basic electrochemical set-up with a working electrode (WE) and counter electrode (CE) connected to an ammeter and a power supply. The WE and reference electrode are connected to a voltmeter to measure the potential changes.

Changing the potential over the cell will have effects both on the reactions occurring and the surface where the reactions occur. One common tool to study electrochemical behavior is voltammetry, where the potential is linearly varied in the electrochemical cell to study changes in the measured current. The result can be connected to different reactions, and voltammetry can be combined with, for example, other types of surface measurements. Cyclic Voltammetry (CV) is a technique where the potential is linearly increased to a specific value and then lowered. It is common to study the behavior of materials during CV to understand the connection between the electrochemical reactions and the properties of the material. Since there can be surface changes caused by the varied potential, which may influence the reactions at the surface, the electrochemical interface is of interest. This interface between the conducting materials is only a few nanometer thick and has effects that may influence the result, even in large-scale applications[1]. The electrode structure is important for increasing the stability and efficiency of electrochemical reactions. Although the electrocatalysts used in technologies such as fuel cells are complex, multifaceted surfaces, detailed surface studies of single-crystal model electrodes provide a better understanding of the system[2]. Therefore, a fundamental understanding of the surface at the atomic level is important.

The reactions studied at the atomic level can be utilized for larger-scale applications. The growing need for sustainable energy and the desire for more advanced technology is fueling the development of modern materials and methods. Nanowires are one such technique that can be used in both nano-electronics and in fuel cells as an electrocatalyst[3, 4]. An area of interest is to create nanowires of new materials with interesting properties. Combining materials that can be used in electrocatalysis with a nanowire structure would lead to a larger area of interaction and thus has the potential to increase efficiency. As the materials become more advanced, the fabrication processes become more complex. Therefore, there is a need for a fundamental understanding of electrochemistry but also a development of the synthesis of new materials to enable new applications. The first part of the project will be a High Energy Surface X-Ray Diffraction (HESXRD) study of the reconstruction of a Au(110) surface and how the surface reconstruction varies with potential and electrolyte. This part will study the atomic arrangement changes of the surface during small changes in the electrochemical environment, which focuses on a fundamental understanding of surface behavior. A second part of the project will study how similar reactions can give major surface changes that can have great applications. In this part, the formation of nanoporous aluminum oxide on an aluminum surface during anodization is studied. The resulting nanopores are subsequently filled by electrodeposition of a metal resulting in metal nanowires.

# 3 The Goals of the Project

The common goal of this project is to study the surface structural changes during electrochemical reactions. The project then consists of two parts which will have their background and goal described separately.

## 3.1 High energy surface x-ray diffraction study of the Au(110) surface

Single crystal plates of gold are often used as electrodes due to their stability and simple use. Other surface orientations, Au(111) and Au(100) are well studied in electrochemical processes. Au(100) has been studied both in vacuum and aqueous solutions and exhibits a hexagonal reconstruction at negative potentials[5, 6]. Au(111) shows a herringbone reconstruction, which is also hexagonal, in a 0.1 M $HClO_4$ electrolyte[2]. The surface structure is of interest since the atomic arrangement has a large impact on the electrochemical properties of the electrode. The reconstruction has been shown to affect electrochemical processes such as adsorption on other low-index gold surfaces since the rearrangement can give different electron densities and atomic coordination. To obtain an understanding of the fundamental processes using gold surfaces and other low-index metal electrodes, there is a need to study reconstructions and other surface properties since these affect the surface reactivity[7]. Apart from a fundamental interest, understanding the structure and processes at a single crystal surface can increase the understanding of the complex electrodes used in real applications, which can increase efficiency and lower costs of industrial applications[5, 8].

Some metal FCC (110) oriented surfaces will, under some conditions, show a (1×2) reconstruction. The best model for explaining this has been the missing row reconstruction where every other row in the ⟨001⟩ direction is missing[9]. Two of the four atoms will be missing in the unit cell in the surface layer, and the others will be relaxed. There will also be structural changes in the second and third layer due to the atoms moving out of the way of the relaxing top layer[10]. Removing every other row at the surface can seem like a large change, but it is energetically beneficial since it can relieve the surface tensile stress[8]. The Au(110) surface is well studied in vacuum, where it has shown a (1×2) missing row structure. This structure can then increase to other higher-order structures such as (1×3) depending on the environment and adsorption at the surface. In liquid electrolytes the Au(110) has shown both (1×2) reconstruction and (1×3) or (1×5) reconstructions under different conditions[8, 11]. It has been shown that changing the applied potential over an electrochemical cell with a Au(110) electrode can change the surface structure[8]. The higher-order structures can be connected to adsorption, just as in vacuum conditions. The adsorption of anions has been shown to induce higher-order faceting and lifting of the reconstruction at higher and lower potentials[5]. There are previous studies performed with $HClO_4$[8] and $H_2SO_4$[7] as the electrolyte, but there is further analysis to be done. There is a need to further understand the dynamics of the reconstructions of Au(110) to deepen the knowledge of gold as an electrode in electrochemical processes. This part of the project aims to investigate the dependence of the Au(110) surface structure as potential is varied using HESXRD.

## 3.2 The electrodeposition of Sn and Pt into porous alumina

Nanowires are commonly manufactured through lithographic methods, which are limited in scale and efficiency. To facilitate and expand future applications for nanowires, methods where the wires are grown, should be developed. One such method is electrochemical deposition, where the structures are formed atom by atom. The electrodeposition can be combined with a nanoporous alumina template, created using anodization, to provide a method that can be efficient and gives fabrication that is not limited to small sizes. Electrodeposition into porous alumina already has extensive use in industry due to the color-changing properties where even small amounts of material in the pores will, due to light scattering interference effects, lead to coloring of the sample[12]. Another aim is to use the nanowires created in electronic applications such as magnetic storage devices, solar cells, and electrocatalysts[12, 13].

Porous alumina templates and deposition of single metals have previously been performed, and pore and wire parameters such as width and wire structure have been studied[14, 15, 16]. The synthesis of bi-metallic nanowires is a new and relatively unknown area. There are alloys with interesting properties that could, for example, be used as electrocatalysts. However, the synthesis of bi-metallic wires comes with a new set of challenges, such as balancing the deposition rate of the ions. The fabrication process and electron deposition for the individual metals must be well understood and stable before a combination is possible. A further development of the fabrication process is to test an asymmetric pulsed deposition, which has previously only been performed in a few cases[17, 18]. However, the comparison to the symmetrical deposition is lacking. This part of the project aims to manufacture Sn and Pt nanowires via electrochemical deposition into nanoporous alumina. The wires will then be studied *ex situ* using a combined focused ion beam and scanning electron microscopy. The goal is to develop a stable manufacturing process for such nanowires to be able to produce bi-metallic wires in the future.

# 4 Theory

## 4.1 The Au(110) and its surface reconstruction

To describe the surface changes during reactions, there must be an understanding of crystalline structures. Therefore, the description of the crystal will begin with definitions related to the bulk of an infinite crystal to further describe the unique properties and dynamics of a surface.

### 4.1.1 Bulk structure

An ideal crystal is a three-dimensional solid built of periodic identical building blocks. The periodicity of any single crystal can be described using the Bravais lattice. This is an infinite lattice where atoms are placed in the lattice points. The basis vectors in the lattice can be described

$$\mathbf{R} = m_1\mathbf{a}_1 + m_2\mathbf{a}_2 + m_3\mathbf{a}_3 \tag{2}$$

where $\mathbf{a}_n$ are vectors, often known as lattice parameters, and $m_n$ are integers. These lattices can be used to describe any ordered crystalline structure. A unit cell describes a

volume that, when translated along the vectors, can fill the whole volume of the crystal[19, 20, 21]. An example of a Bravais lattice can be seen in Figure 2a.

When measuring crystalline structures, one will encounter the reciprocal space. This is the Fourier transform of the real space Bravais lattice and is defined as the set of vectors that fulfills

$$\mathbf{R} \cdot \mathbf{G} = 2\pi n \tag{3}$$

where $n$ is an integer. This should be true for any $\mathbf{R}$ and $\mathbf{G}$, that can be defined

$$\mathbf{G} = m_1' \mathbf{b}_1 + m_2' \mathbf{b}_2 + m_3' \mathbf{b}_3 \tag{4}$$

where $m_n'$ are integers and $\mathbf{b}_n$ are the vectors spanning the reciprocal lattice, a new Bravais lattice[19]. This can be seen for a simple rectangular lattice in Figure 2b.



(a)

(b)
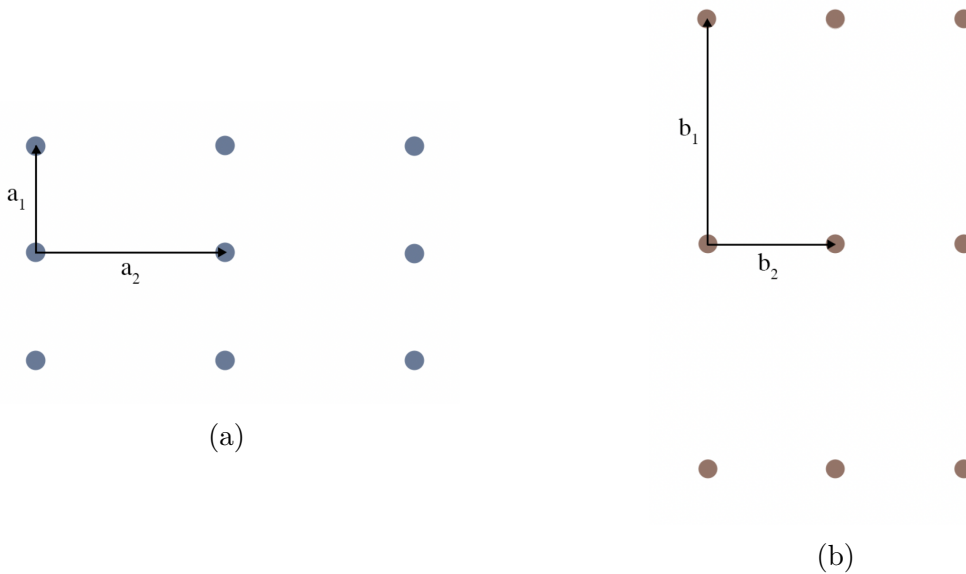
**Figure** 2: (a) A two-dimensional Bravais lattice with a rectangular unit cell. (b) The reciprocal space lattice of the crystal in (a). The vector lengths will relate $|\mathbf{b}_1| = 2\pi/|\mathbf{a}_1|$ and $|\mathbf{b}_2| = 2\pi/|\mathbf{a}_2|$.

For metals, it is energetically beneficial to have a large orbital overlap. Therefore, metals often have tightly packed structures. One of the most common crystalline structures is the Face-Centered Cubic (FCC), which can be seen in Figure 3a. The cubic structure with an additional atom at each side gives a high packing density. The orientation of the crystal is often of interest, and there is thus a need to define different lattice planes. These planes are defined by Miller indices that are defined by the reciprocal value of where the plane intersects the crystal axis in units of lattice vectors[19, 20, 21]. The 110 plane for an FCC crystal can be seen in Figure 3b. The figure also shows the two-dimensional 110 plane that will have a rectangle unit cell.

(a)



(b)
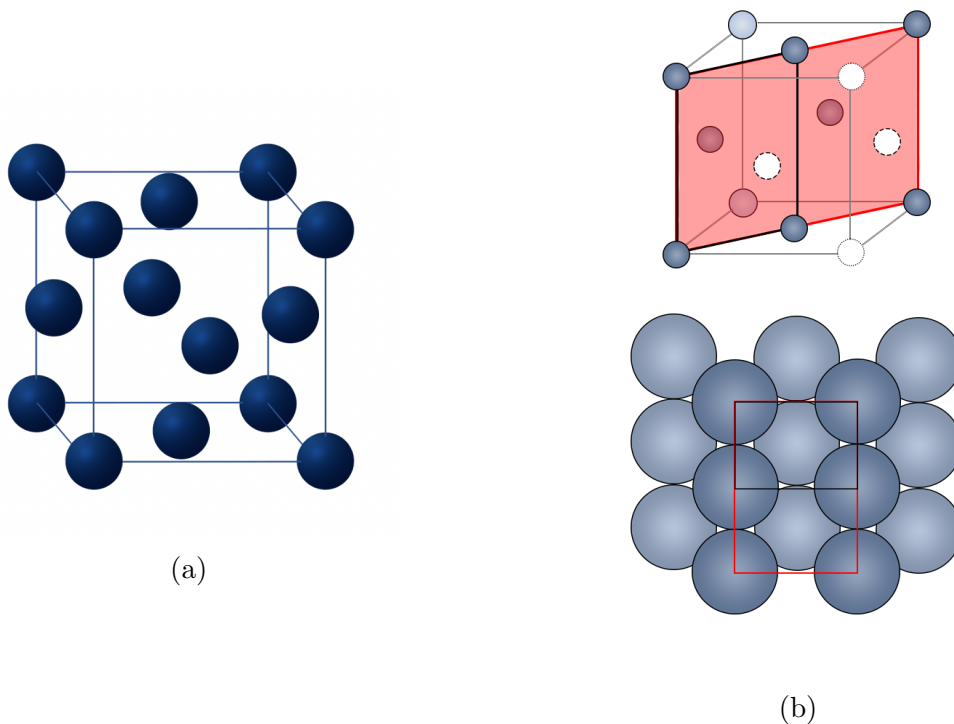
**Figure** 3: (a) A schematic image of an FCC crystal. The blue balls represent the atoms. (b) The (110) plane on the FCC crystal. The bottom figure shows the same black and red rectangle but in the 110 plane of the crystal.

### 4.1.2   Surface structure and reconstruction

Since no real crystal is infinite, all crystals will have a surface that will have different properties compared to the bulk[19]. When discussing the surface, the top three atom layers are often considered since they experience such different conditions that they differentiate from the bulk or the substrate. A surface is unreconstructed if the surface atomic arrangement is the same as the bulk, with the exception of relaxation, which is a change in distance between the topmost atom layers that almost always occur. However, the relaxation will not affect the primitive unit cell of the surface, unlike the reconstruction where a new surface structure, and thus a primitive unit cell, is created to minimize the surface free energy. The reconstructed surface can have the same or a different amount of atoms compared to the bulk and can also have different orientations and symmetries compared to the bulk structure. A reconstruction of the sample often occurs under specific conditions. It can thus vary depending on different parameters such as pressure and potential since, for example, the addition of extra electrons can change the environment for the atom such that it is more similar to the one in the bulk[15, 20].

One common reconstruction is the formation of small steps of more energetically beneficial surfaces. This formation can significantly affect the surface properties since the edge-atoms can be undercoordinated and have different surface properties affecting the adsorption and desorption of molecules[20]. The missing row reconstruction of an FCC (110) surface entails that every other row in the $\langle 001 \rangle$ direction is removed. There can also be higher-order missing row reconstructions where more rows are removed[8]. The relaxed (1×1) surface, the (1×2) missing row reconstruction, and the (1×3) missing row

reconstruction can be seen in Figure 4. Changing the sample environment can induce transitions between reconstruction orders. During the transition, surfaces have been observed to be in an intermediate rougher state, which is known as transition roughening[22].

(1x1) (relaxed)　　　　　(1x2) (reconstructed)　　　　　(1x3) (reconstructed)

Top view

Side view
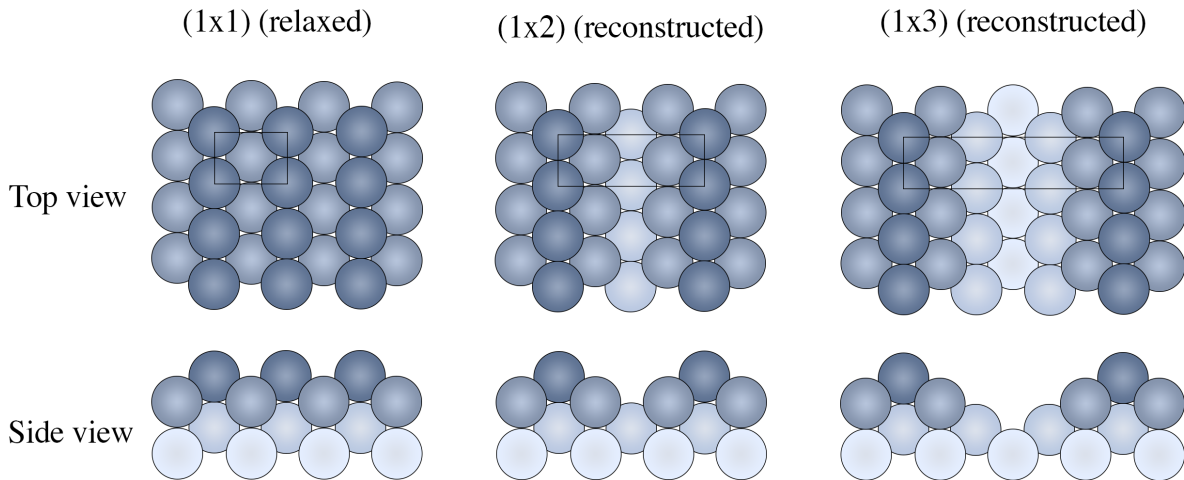
**Figure** 4: A schematic figure of a relaxed FCC (110) surface (left), a (1×2) missing row reconstruction (middle) and (1×3) missing row reconstruction (right). The black box shows the unit cell for each surface structure.

### 4.1.3 The Au(110) surface

Gold has an FCC structure, and Au(110) has a rectangular unit cell with the sides $a_1 = 4.08$ Å and $a_2 = 2.89$ Å. Scanning tunneling microscopy (STM) and other in-vacuum methods have shown that the surface reconstructs into a (1×2) structure. There have been reports of higher-order reconstructions, where (1×3) or (1×5) have been observed after extensive annealing or other environmental changes. The (1×2) missing row structure has been shown to form stable, large, defect-free domains. The formation of higher-order structures has, in vacuum, been shown to be connected to the presence of impurities and has a higher presence of terraces and kinks. Larger (1×3) domains and the presence of (1×5) or (1×7) reconstruction require higher amounts of adsorbed impurities[23]. The surface reconstruction has been shown to be temperature-dependent for clean Au(110) in Ultrahigh Vacuum (UHV), with (1×2) being the most stable at low temperatures[8].

Studying the surface structure under electrochemical conditions is more complex. An electrode potential dependence has been shown for Au(110) in $HClO_4$ where the surface has shown a (1×2) reconstruction at 0 V and then transformed into a (1×3) reconstruction at lower potentials[8]. Studies of Au(110) in $H_2SO_4$ have shown that domains of (1×2) and (1×3) structures exist in parallel under negative potentials while no clear reconstruction was shown at positive potential[7]. Also, in the electrolyte environment, the higher-order reconstruction and lifting of the reconstruction seem to be connected to adsorption. This can be both adsorption of anions from the electrolyte but also coadsorption of anions from the electrolyte and anions created in the electrooxidation[5].

## 4.2 Electrodeposition into porous alumina

Porous alumina templates can be used to form nano-scale wires by depositing material into the pores. Electrochemical anodization is used to form Porous Anodic Alumina (PAA) and allows for control of pore size and distance. Using electrochemical deposition removes limitations of sample size in production. It is also an efficient way of producing wires from many different materials. The pore properties can be varied by changing preparation parameters. This can be the size of the pores, the pore density, and the hole packing structure. The nanowire diameter can be varied by changing the anodization parameters, and it is then possible to control the wire length by changing the deposition time[16]. The deposition of material in the PAA templates has possible applications as nano-scale devices such as magnetic storage devices, solar cells, and electrocatalysts. If the alumina is removed, it can leave freestanding structures[13]. This section will describe the PAA formation, electrochemical deposition, and the wire materials used in this project.

### 4.2.1 Porous alumina

An oxide is formed on an aluminum surface when exposed to air. This oxide will naturally be between 1.6 and 2.5 nm thick[24]. A thicker oxide can be created through anodization. The oxide can be either homogeneous or porous, depending on the anodization environment. If the electrolyte is acidic, such that the oxide layer is soluble in it, pores will form. There is not a conclusive reason for this, but two suggested explanations have been proposed: either dissolution of the oxide or that the pores are caused by stress[12]. By varying the anodization potential, temperature, and acidity, the oxide thickness and pore diameter can be varied[25]. The pores in porous alumina can have diameters of 10-200 nm and be several $\mu$m deep. The pore diameter has previously been shown to be approximately 25 nm when the PAA template was anodized in 0.3 M sulfuric acid and 40 nm when prepared in 0.3 M oxalic acid[14].

Under some conditions, the pores can be self-organized in a hexagonal pattern. This occurs when the anodization is performed close to the breaking potential, which will depend on the electrolyte used[12]. The pore order will increase with time, making the pores more ordered at the bottom than at the oxide surface. To create a more well-ordered PAA, one can use two-step anodization. In two-step anodization, the oxide layer is stripped with a chemical etch after the first anodization, leaving the aluminum surface with well-ordered nanoconcaves. Using this aluminum surface in a second anodization step will leave a highly ordered PAA[12, 14]. A schematic drawing of the two-step anodization can be seen in Figure 5.

### 4.2.2 Electrochemical deposition

Electrodeposition is a bottom-up method where the wires are grown atom by atom inside the pores. Applying a potential over an electrochemical cell with the PAA template as the working electrode will lead to reduction of the ions in the solution at the bottom of the pores. This is the ideal description of the electrodeposition, and there will, in reality, be several issues that are needed to overcome: the thick barrier layer, charge buildup, and mass transfer limitations[14], all shown in Figure 6.

The growth of the PAA will result in pores with a barrier layer, an insulating layer of aluminum oxide separating the pore from the aluminum bulk. The electrodeposition will not occur unless electrons can tunnel through the barrier layer. The tunneling coefficient
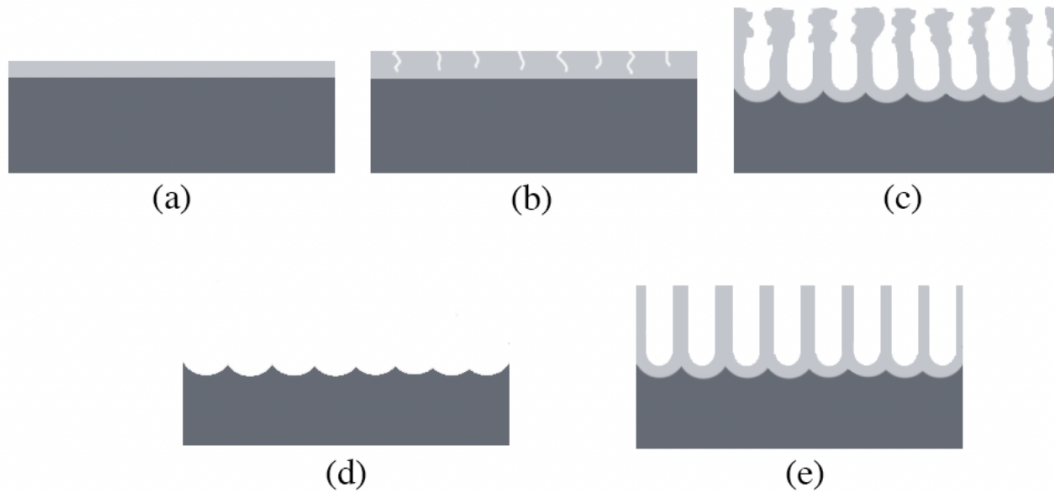
**Figure** 5: (a) The aluminum surface with the natural thin oxide layer. (b) The thicker oxide from anodization with some unordered small pores. (c) Pores after one anodization step. The order will increase with time, and the bottom of the pores will thus be more well ordered than the top. (d) The surface with nanoconcaves after the oxide has been stripped with a chemical etch. (e) The surface after the second anodization step with well-ordered pores.

(i.e. probability of electrons tunneling through a barrier) can simplified be described $T \propto e^{-d}$ where $d$ is the distance. Since the tunneling probability is distance-dependent, the thick barrier layer will hinder the electrodeposition. There are two main methods to overcome this issue. The first is pore widening, etching away some of the barrier layer with a chemical etch. Phosphoric acid is commonly used as the chemical etch. However, this method will also lead to a larger pore diameter and not just etching of the barrier layer. There is also a risk of destroying the template if left in the etch too long. The second method is electrochemical barrier layer thinning. The barrier layer thickness will be dependent on the anodization potential. By slowly lowering the potential at the end of the second anodization, smaller pores with a thinner barrier layer will form at the bottom of the pores. These branches of smaller pores will enable the electrodeposition[14].

After barrier layer thinning, there is a thin insulating oxide layer regardless of thinning method. Direct current (DC) will lead to charge buildup, and result in non-uniform deposition. Alternating current (AC) electrodeposition overcomes this issue. However, the deposition will quickly lead to mass transfer limitation since the recovery of the ionic species to the bottom of the pores will be slow. The recovery time is even longer since the diffusion is slower in the pores than in the bulk of the solution. Therefore a Pulsed Electrodeposition (PED) with long of-time is commonly used[12, 14]. Although the positive part of the pulse is necessary to avoid charge buildup, there have been reports of the anodic pulse dissolving electrochemically deposited material. A symmetrical pulse is more common, but successful deposition has been achieved with a smaller or shorter positive pulse[17, 18].
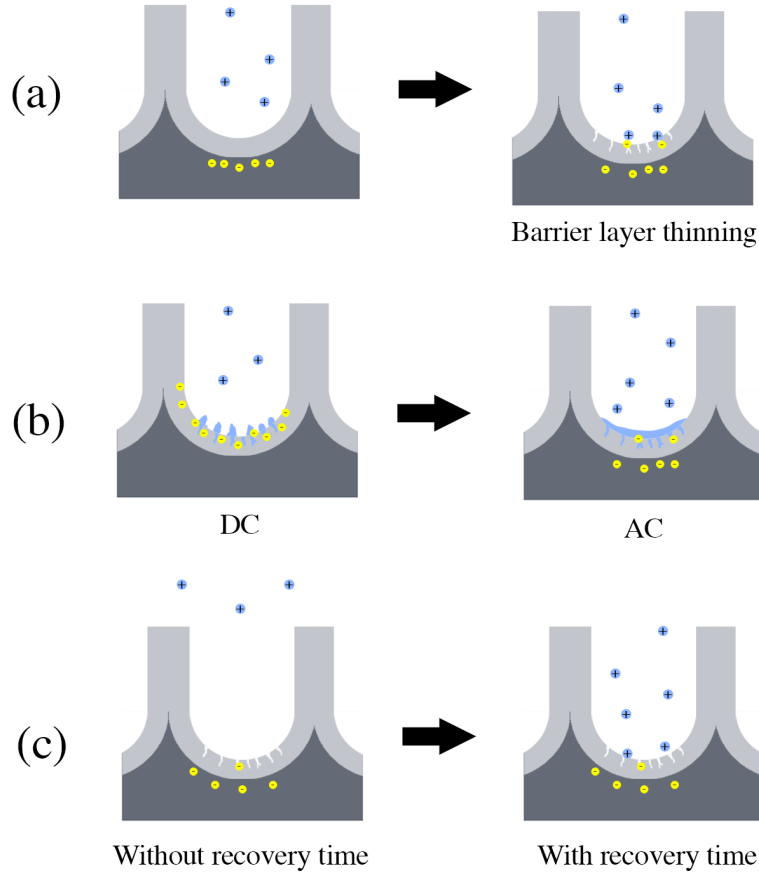
**Figure** 6: Schematic image of electrodeposition into a pore. The light gray is the barrier layer, the blue balls represent the ions and the yellow the electrons. (a) The template with the thick barrier layer with low tunneling probability. The issue is solved by for example barrier layer thinning where small pores are formed. (b) DC will give charge buildup in the barrier layer leading to uneven deposition. The positive part of an AC will discharge the barrier layer. (c) If a sine potential is used for deposition, the slow diffusion of ions into the pores will result in the deposition being limited by the lack of ions. If a pulsed potential with a long recovery time is used, the deposition will no longer be mass transfer limited.

### 4.2.3 Low-dimensional metals in PAA

One of the most studied materials for nanowires is tin (Sn) due to the properties of the material, such as good conductivity and corrosion resistance. Sn has had a large use as wires and solders in electronics. Nanowires of Sn have previously been shown to exhibit great superconducting and magnetizing properties and can thus have several electronic applications. PAA filled with Sn has a black finish, so it has applications in aluminum coloring. The Sn nanowires have been studied both *ex situ* with the template removed and *in situ* during the growth process in the PAA template[13, 15]. The reduction of Sn can be describes by

$$Sn^{2+} + 2e^- \rightarrow Sn. \tag{5}$$

Platinum (Pt) is also a metal with good corrosion resistance and a material that has been of interest in PAA due to its catalytic properties[15]. Pt nanowires have been

fabricated via DC and AC deposition[26, 27]. The reduction of Pt can be writen as

$$Pt^{2+} + 2e^- \rightarrow Pt. \tag{6}$$

Pt works as a catalyst in, for example, CO oxidation and electro-oxidation of alcohols, which can all be improved by the addition of Sn[28]. A reason to study these two metals is their interesting potential as alloy nanowires. Pt-Sn is used as bi-metallic catalyst when reforming hydrocarbons. This process takes low-quality carbon structures and transforms them into fuel with high-quality combustion properties[29]. An interesting development of these bi-metallic materials is the use of alloy nanowires to increase the contact area.

## 4.3   Experimental Tools

The first part of the project entails HESXRD measurements utilizing synchrotron radiation. The basics of synchrotron radiation, the Swedish beamline P21 2 at DESY in Hamburg, and HESXRD will be described here. For the second part of the project, a combined focused ion beam (FIB) and scanning electron microscope (SEM) were used to study the nanowires.

### 4.3.1   Synchrotron radiation and the beamline

Light as a tool to study materials is not new but stems back to 1800. Scientists then started with only visible light, which is limited to the energy range of 1.75 eV to 3.2 eV. X-rays were then discovered in 1895. X-rays are electromagnetic radiation with energies between 100 eV to 100 keV, with the lower part of the spectra being referred to as "soft x-rays" and the higher "hard x-rays". As science advanced, there has been a need for more careful measurements, pushing the development of x-ray sources. Lab sources for x-rays (x-ray tubes) are limited to a small energy range depending on their anode material. It has also been difficult to achieve small beams and high resolution. Therefore, many experiments require synchrotron x-ray sources which can have a higher intensity, resolution, and a tunable energy range[15, 30].

In a synchrotron, the light has circulating electrons in a ring as its source. Electrons are injected into the ring by an electron gun that are initially accelerated using a Linear Accelerator (LINAC). The electrons are also separated into small electron bunches in the LINAC before entering the storage ring. The energy of the electrons in a storage ring is constant at some GeV. The electrons would, without interference, continue in a straight path. Therefore, the storage ring has magnets bending the electron path and shaping the clusters through the Lorentz law. Focusing magnets are required since the electrons in the bunch will repel each other[30]. Light will be emitted at the bending magnets due to the inward acceleration of the electrons. In the first synchrotron facilities, this was the light used for experiments. In modern facilities, insertion devices known as wigglers and undulators will make the electrons oscillate in a straight path. The resulting light will be of higher brilliance than that achievable with a bending magnet. The light will continue into a beamline where optical components will tune the beam to the requirements of the method at that beamline[15, 31].

One modern light source is PETRA III at DESY in Hamburg. It is a 6 GeV storage ring that became operational in 2009. One of the beamlines is the Swedish beamline P21 which is aimed at high energy x-ray material science. There are two branches, one for broadband diffraction (P21.1) and one for diffraction and imaging (P21.2)[32]. The

beamline set-up and optics can be seen in Figure 7. The beamline has an energy range of 40-150 keV and can combine Small-Angle X-ray Scattering (SAXS) with Wide-Angle X-ray Scattering (WAXS)[33].
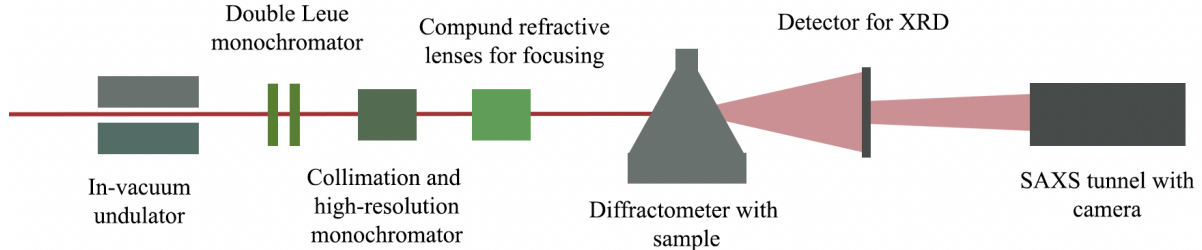


**Figure** 7: A schematic image of the set-up of P21.2. The x-ray beam is produced by an in-vacuum undulator. The beam then passes through two monochromators. First, a broadband double Laue monochromator, and then a collimator and high-resolution monochromator with an energy range of $40 - 100$ keV. The beam is focused with compound refractive lenses, which can be placed at different positions to achieve different focusing. The sample is placed on a diffractometer, and the diffracted beam is detected by a number of detectors which can be combined with a detector at the end of a SAXS tunnel.

### 4.3.2 X-ray diffraction

Diffraction can give information about unknown structures in material science. It is ideal to use for crystalline structures since it is sensitive to periodic atomic structures[21]. Diffraction measurements can be performed using different particles such as electrons or neutrons, but here X-Ray Diffraction (XRD) is used. The x-rays that interact with the atoms will give rise to a diffraction pattern through interference by the scattered x-rays. The positive interference peaks are known as bragg peaks[15]. When working with the diffraction of x-rays, it is assumed that the incoming wave induces a spherical wave for each point $\mathbf{r}$ in the material. Coherent scattering is also assumed, meaning a fixed phase relationship between the incoming wave and all emitted spherical waves[21]. The oscillating electromagnetic field beam will induce oscillations of the electrons in the material with the same frequency. This oscillation will then emit new x-rays. The interference of the induced fields will then lead to the diffraction pattern. The plane wave of an electric field can be described

$$\mathbf{E}(\mathbf{r}, t) = \mathbf{E}_0 e^{i\mathbf{k}\cdot\mathbf{r} - i\omega t}, \tag{7}$$

where $\mathbf{k}$ is the wave vector. The physical electric field will be the real part of the equation above. The wave vectors of the incoming x-rays $\mathbf{k}$ and the scattered light $\mathbf{k}'$ will have different directions but the same magnitude, if elastic scattering is assumed[20]. The intensity of the field is obtained $I(\mathbf{r}, t) = |\mathbf{E}_0|^2$. The diffracted intensity relates to the electron density of the sample, which in turn relates to the atomic structure since the electron density is largest by the ion cores. The diffraction can thus determine the geometry of the atoms in the crystal since this is periodic[19].

The diffraction can be described via Bragg's law or the Laue condition. In Figure 8, the geometry used to explain the Laue condition can be seen, starting the explanation from the interference between two atoms.
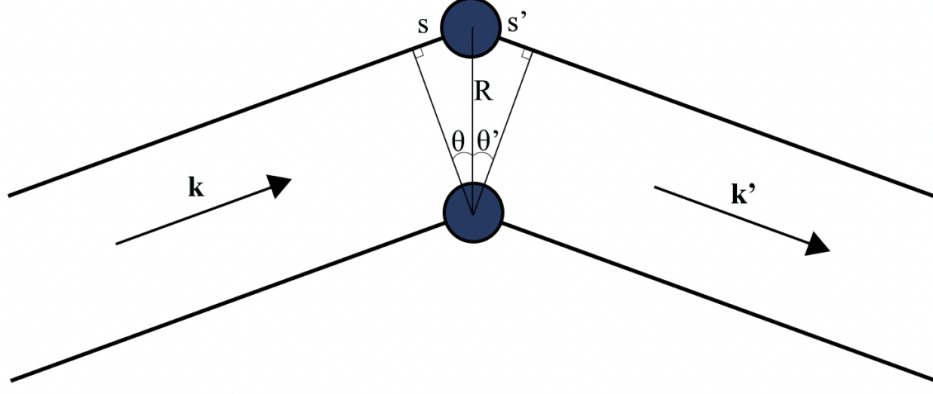
**Figure** 8: The geometry used to explain the Laue condition with $R$ being the atom distance and **k** and **k'** being the incoming and scattered wave vector.

The distance **R** between the two atoms is the lattice vector described in Equation 2. The path difference (PD) needs to be an integer, $n$, of the wavelength, $\lambda$, in order to have constructive interference. This can be described by

$$PD = n\lambda = n\frac{2\pi}{k}. \tag{8}$$

$PD$ will also be the sum of the path difference of the incoming and outgoing x-ray. This will, together with the definitions if Figure 8 give

$$PD = s + s' = \mathbf{R}\cos\theta + \mathbf{R}\cos\theta' = \frac{\mathbf{k}\cdot\mathbf{R} - \mathbf{k}'\cdot\mathbf{R}}{k} = \frac{\mathbf{R}\cdot\Delta\mathbf{k}}{k}. \tag{9}$$

Combining equation 8 and 9 will give

$$\mathbf{R}\cdot\Delta\mathbf{k} = 2\pi n. \tag{10}$$

This defines the conditions for constructive interference with the Laue condition. Further, $\Delta\mathbf{k}$ needs to be equal to the the reciprocal lattice vector **G** according to equation 3. Thus combining equation 10 with the definitions of the real space and reciprocal space vectors in equation 2 and 4 gives

$$\begin{aligned} 2\pi n = \mathbf{R}\cdot\Delta\mathbf{k} &= (m_1\mathbf{a_1} + m_2\mathbf{a_2} + m_3\mathbf{a_3})\cdot(m_1'\mathbf{b_1} + m_2'\mathbf{b_2} + m_3'\mathbf{b_3}) \\ &= 2\pi(m_1 m_1' + m_2 m_2' + m_3 m_3'). \end{aligned} \tag{11}$$

What equation 11 shows is that, within these condition, the $m_n'$ needs to be integers and $\Delta\mathbf{k} = \mathbf{G}$. $\Delta\mathbf{k}$ will describe a lattice point that will be measured under specific orientations of the sample and detector. This can be described by the Ewald sphere, which can be seen in Figure 9, where the magnitude $k$ of the vector **k** is the radius. The vector **k** will point from the sphere center to a reciprocal lattice point. By changing the sample orientation, a point will intersect with the sphere and thus give constructive interference. Moving the sample to give positive interference and moving the detector to measure in the **k'** direction makes the interference detectable[15].

As already discussed in previous sections, the surface of the crystal can have different properties and structures from that of the bulk of the crystal. It is also at the surface that
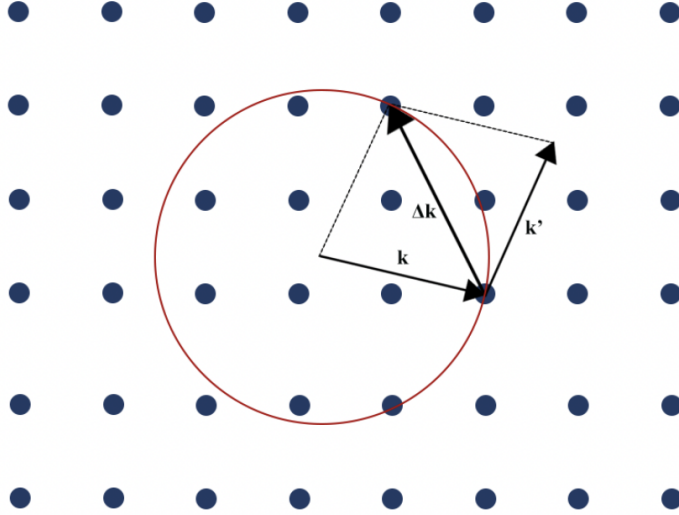
**Figure** 9: An example of an Ewald sphere on a square lattice.

many reactions occur since it is the interface between the crystal and the surrounding. There are special requirements for Surface X-ray Diffraction (SXRD) measurements since the bulk of the crystal is much larger than the surface and will thus have a higher signal. One requirement is the use of synchrotron radiation to have a strong enough signal. A small incidence angle is used to minimize the signal from the bulk. Most materials have a negative refractive index for x-rays. Hence, as an x-ray beam travels from a less dense to a denser material, grazing incidence angles can give total external reflection. Therefore using an angle near or below the critical angle for the used energy and material will limit the penetration depth of the x-rays. The diffraction pattern of a 2D structure will be lattice rods with a continuous intensity perpendicular to the 2D structure. This stems from the periodic structure in the horizontal plane, but the structure is finite in the vertical direction. Since the material is not a 2D structure, the surface diffraction will be a combination of bragg peaks and lattice rods known as a Crystal Truncation Rod (CTR). Looking along the CTR, the signal between the bragg peaks can give information about the surface structure. If the surface structure is different from the bulk structure, there will be rods visible between the CTRs known as Superstructure rods. These will have a different periodicity than the bulk and will thus not intersect with the bragg peaks. Analyzing the position of these peaks will give information about the surface structure[15].

SXRD measurements can be performed using low-energy x-rays and moving the detector around the sample as the surface is rotated/tilted. For this method, filters are put in the x-ray beam at the reciprocal space location for the bragg peaks, or these locations are avoided not to saturate the detector. Another approach is to have a larger detector in the x-ray beam direction after the sample. Then, as the sample is rotated, a full reciprocal space image of the sample will be detected. Higher energies can be used for this, and the measurements are often referred to as High Energy Surface X-ray Diffraction (HESXRD). To protect the detectors from the intense bragg peaks, beam stops are often placed on the detector at the location of reciprocal space while the x-ray beam is not at full intensity[15]. An example of a HESXRD measurement can be seen in Figure 10.

If a sample has crystalline grains of different orientations, such as a polycrystalline sample, it will have many directions where the diffraction criteria are met instead of rods.

This will show up as circular patterns known as powder rings. If there are powder rings in a single crystal measurement, they are indicators of imperfections in the crystalline structure.
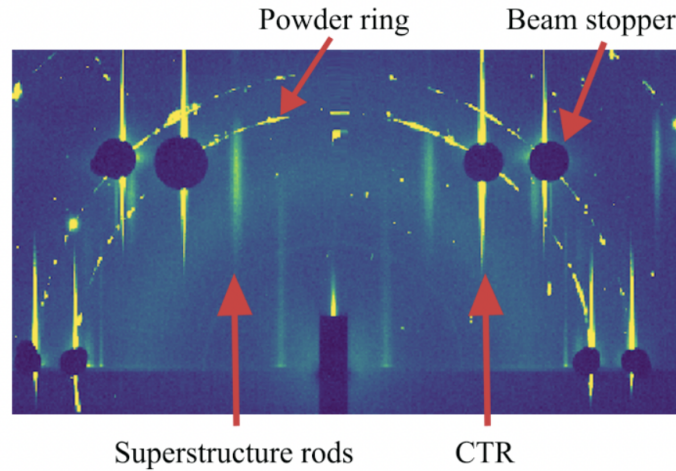


**Figure** 10: An example of a HESXRD measurement with indicated powder ring, beam stopper, CTR, and superstructure rod.

### 4.3.3 Surface optical reflectance

Surface Optical Reflectance (SOR) is a method where the reflected light of a collimated LED is measured. The intensity of the reflected light will depend on the surface roughness, which can give an idea of reactions at the surface. The method is often combined with other methods, such as SXRD, to get a macroscopic impression of the surface combined with the atomic structure[2, 15].

### 4.3.4 Scanning electron microscope

In a scanning electron microscope (SEM), a focused beam of electrons is used to scan the surface[34]. This can give information about the surface structure and chemical composition. The primary electrons (PE) from the electron beam will give rice to secondary electrons (SE) when the surface is bombarded. The rate of SE will depend on the material of the surface and the surface topography. These low-energy SE will have a short escape depth, and the SEM is thus highly surface sensitive. The sensitivity will depend on the penetration depth of the electrons, which will both depend on the electron energy and the material properties, such as the atomic number. The detected SE will be from 5-10 nm into the sample. There is also the possibility to detect backscattered electrons which will differ between different materials due to their different scattering intensity[12]. Bombarding the surface with electrons can also give rise to x-rays and Auger electrons, but this will not be further discussed in this project. The possible outcomes of a PE can be seen in Figure 11.

A schematic image of the SEM set-up can be seen in Figure 11. The SEM is used in vacuum to minimize the unwanted scattering. The electrons will be emitted from an electron gun with a heated filament, where the heating current will determine the number of electrons. The electrons will then be accelerated via an applied potential between

the electron gun and an anode. The beam will, after the acceleration, be shaped and focused using a series of electromagnetic apertures. The focused beam is then raster-scanned over a part of the sample. A bias is used between the sample and the detector to collect electrons. The collected electrons will then create an image of the surface by first converting the electron signal to light in a scintillator which will be amplified in a photomultiplier tube which gives a voltage readout[12].



(a)

(b)
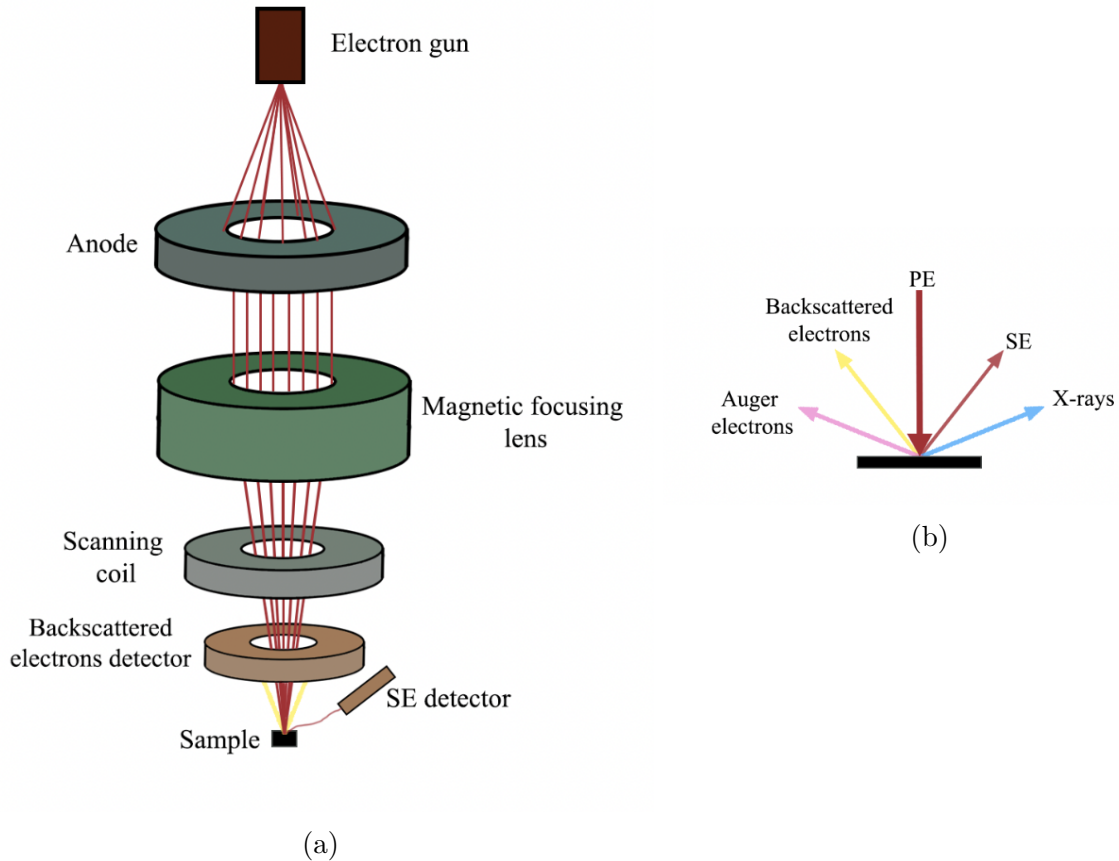
**Figure** 11: (a) A schematic image of the parts of an SEM. The electrons are emitted by an electron gun and accelerated via an anode. The electron beam is then focused by magnetic lenses and scanned over the sample using a coil. The backscattered and SE electrons are then detected. (b) The outcomes of electron-material interaction where the PE can give rise to SE, backscattered electrons, Auger electrons, or x-rays.

### 4.3.5 Focused ion beam

The basic set-up of the Focused Ion Beam (FIB) is similar to that of the SEM. Instead of electrons, the FIB uses gallium ions ($Ga^+$) generated by applying a strong electric field to a liquid-metal ion source. The electric field extracts the positive gallium ions from the liquid gallium, which are then shaped into a beam through a series of electrical lenses. An octopole is used to scan the beam over the surface. The focal spot is usually in the range of 10 nm. The beam current can be varied for different applications, but a higher beam current can cause more significant surface damage. To limit the scattering of the ions, the FIB is used in UHV. The FIB can be used for imaging by measuring

the SE and secondary ions emitted when the beam scans the surface. However, the main uses of the FIB are milling and deposition. When milling, a high ion current is used to sputter sample material. This can be done with high precision to get milled shapes on the surface. For deposition, a chemical vapor of the desired material, often a metal, is used in combination with the FIB. The deposition will occur through the principle of chemical vapor deposition. The vapor from a thin nozzle will adsorb to the surface. The high current ion beam decomposes the adsorbed gas leaving a thin film of the desired product at the surface[35].
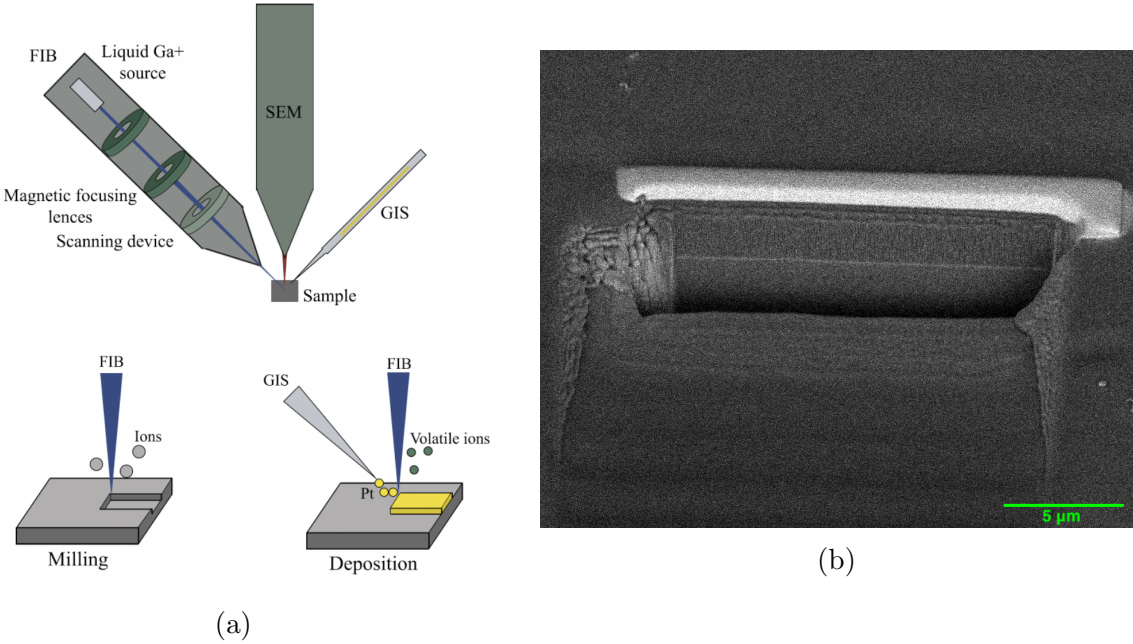


**Figure** 12: (a) A schematic drawing of a FIB set-up with an SEM and Gas Injection Device (GIS) (top). A drawing of FIB milling and Pt deposition (bottom). (b) An SEM image of FIB milling. The lighter part is a Pt strip deposited on the surface.

# 5 Result and Discussion

## 5.1 High energy surface x-ray diffraction study of the Au(110) surface

HESXRD from the Au(110) surface was measured at the Swedish beamline 21.2 at PETRA III at DESY during two different beam times.

### 5.1.1 Experimental set-up

The diffraction was measured with one or two Perkin-Elmer flat panel x-ray detectors with 2880×2880 pixels and 150×150 $\mu$m pixel size. One detector was used at the first beamtime and two at the second. Beam stops were placed on the detector at the bragg reflections to protect the detector. The x-ray beam had an energy of 67 and 68 keV at the first and second beamtime, respectively, and a grazing incidence angle of 0.07°, the critical angle for Au at these energies.

The electrochemical cell set-up can be seen in Figure 13. The electrochemical cell was a PEEK electrochemical flow cell further described by W. Linpé et al.[36]. The top part was replaced with a fused silica window to allow SOR measurements. The SOR set-up was a LED collimated and directed at the sample through a series of lenses and apertures. A CMOS camera captured the reflected light after a series of lenses. A potentiostat was connected to a brass connector in contact with the sample and the polycrystalline gold CE. The reference electrode was an eDAQ miniature Ag/AgCl electrode. All potentials given will be in reference to the Ag/AgCl reference electrode. All glass ware used for the experiment was cleaned in a Piranha solution (3:1 98 % $H_2SO_4$+30 % $H_2O_2$), and the PEEK chamber and parts were cleaned in 30 % $HNO_3$. Both glass ware and chamber were then rinsed and boiled in ultra-pure water.
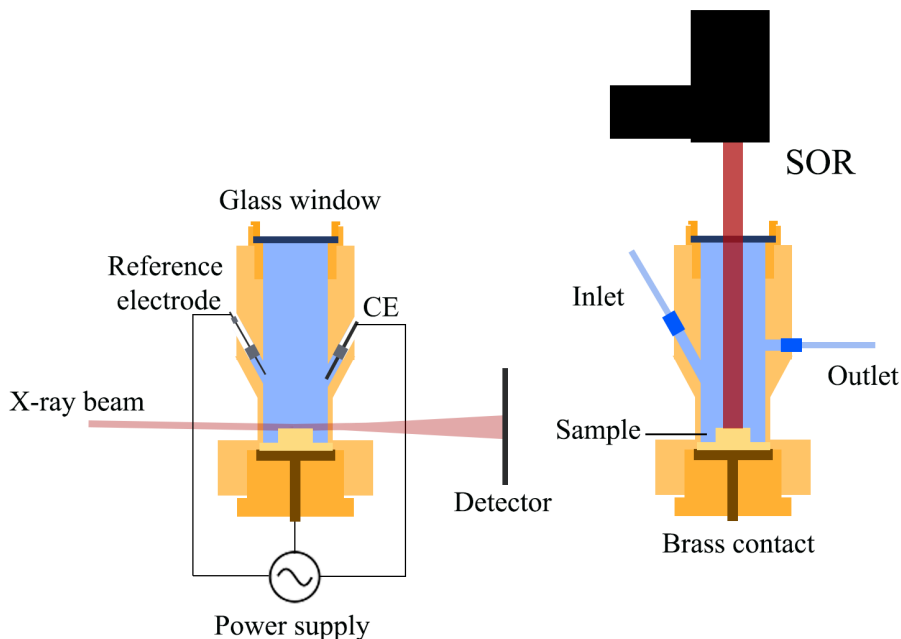


**Figure** 13: A schematic drawing of the electrochemical cell used for HESXRD from two directions. The left one also shows the circuit, the x-ray beam, and the the detector. The right one shows the SOR set-up.

The sample was a single crystal Au(110) surface from MaTecK, prepared by soaking it in 35 % $HNO_3$ and then rinsing it with ultra-pure water. It was then oxidized in 0.1 M $HClO_4$ at 4 V for a few seconds before dipping it in 1 M HCl for 30 s and flame-annealing. A pump was used to flow a 0.1 M $H_2SO_4$ electrolyte or a 0.1 M $HClO_4$ electrolyte through the chamber. Both electrolytes were bubbled with argon throughout the experiments.

The sample was aligned in water. Images of the chamber filled with water without the sample were used as background at the first beamtime. For rotational scans, a series of images (1801 images at first beamtime and 2110 for second beamtime) were captured over a 180° horizontal sample rotation while the potential was constant. For time scans, the sample was set to a chosen angle such that a reconstruction of interest could be seen. A series of measurements were then performed as the potential was varied. This was combined with simultaneous SOR measurements.

### 5.1.2 Data visualization

The sample detector distance and central pixel were calibrated using measurements of a $CeO_2$ surface as a reference in the software package pyFAI[37]. The images were then initially analyzed with the HESXRD Analysis Toolkit (HAT)[38]. A detector image compiled using HAT from the first beamtime with one detector can be seen in Figure 14. The detector image was obtained by adding the 1801 images and using the highest pixel intensity from each angle. The beam stops are visible as black areas in the image. They are covering the bragg reflections, and the lines by the beam stops, the CTRs, will correspond to diffraction from the bulk structure. There are circular lines centered around the beam, which are powder rings. This indicates that the surface near region is imperfect.
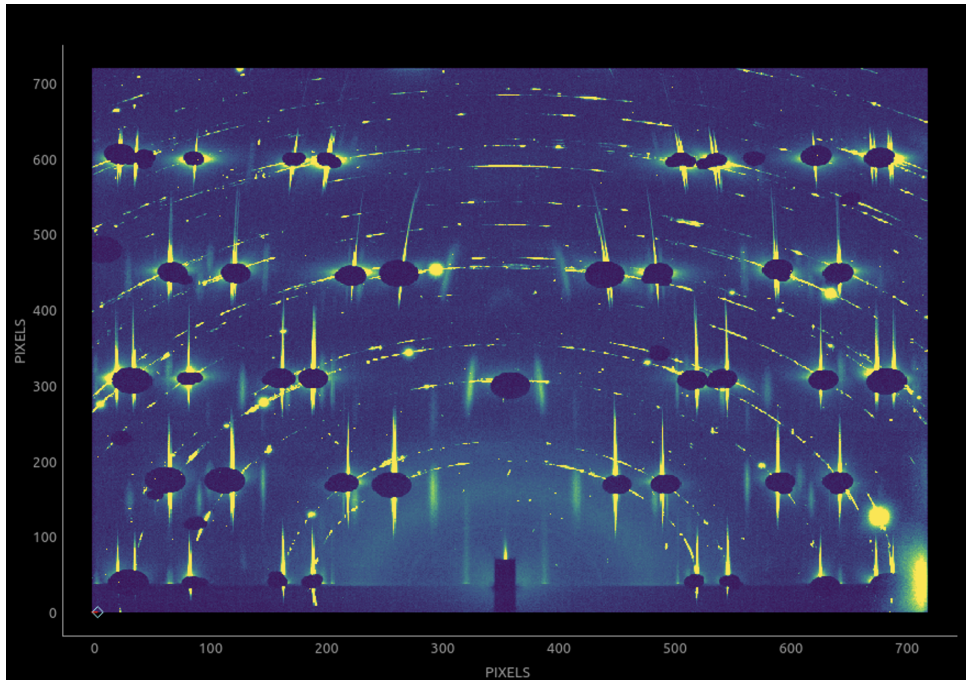


**Figure** 14: A detector image before data treatment of Au(110) in $HClO_4$ at -100 mV vs Ag/AgCl. Black areas are beam stops covering the bragg reflections. The lines corresponding to the bragg reflections stem from the bulk structure of the crystal. The circular lines are powder rings indicating that the surface near region is imperfect. The lines between the CTRs are the superlattice rods from the reconstruction.

Similarly, the detector image from the second beamtime can be seen in Figure 15. Since the second beamtime used two detectors, the image has a gap in the middle with a distance calibrated using the pyFAI software at the same time as the calibration of the central pixel and detector distance. As for the first beamtime, powder rings can be observed, indicating an imperfect single crystal surface.
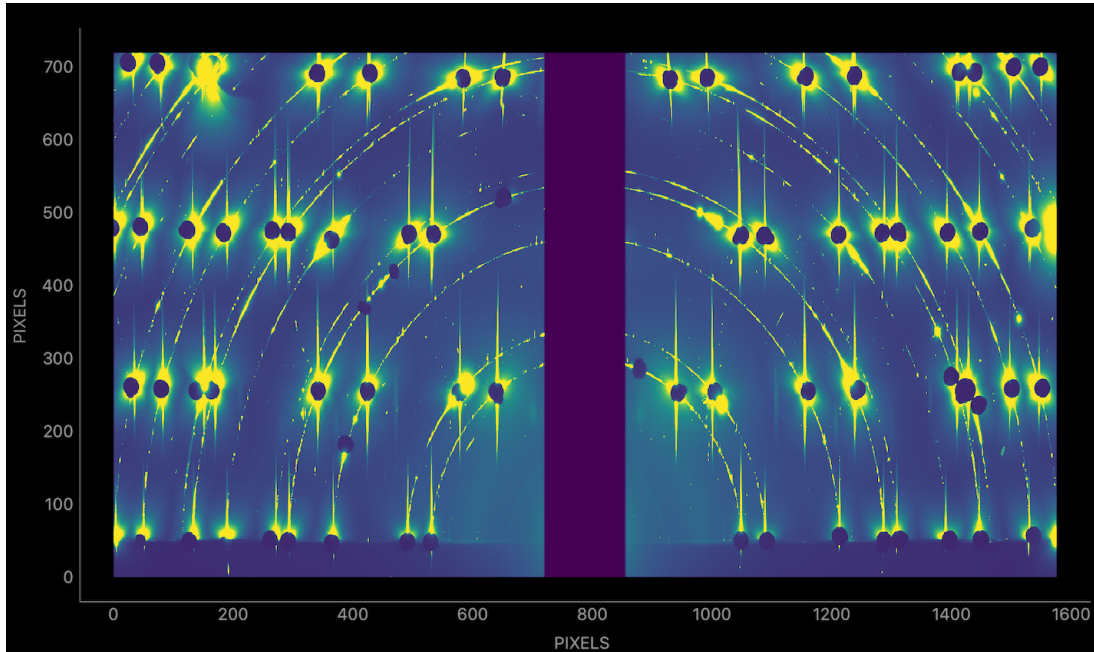


**Figure** 15: A detector image before data treatment of Au(110) in HClO$_4$ at -206 mV vs Ag/AgCl. The image is divided with a gap since two detectors were used at the second beamtime. Black areas are beam stops covering the bragg reflections. The lines corresponding to the bragg reflections stem from the bulk structure of the crystal. The circular lines are powder rings indicating that the surface is imperfect. The faint lines between the CTRs are the superstructure rods from the reconstruction.

### 5.1.3 Data treatment

The HAT was used to transform the detector image into a transformed image in reciprocal space units. This transformation uses the lattice parameters for the crystal, $a_1$, $a_2$, and $a_3$. The x-axis is $\sqrt{H^2 + (rK^2)}$ where $r = a_1/a_2$. This transformed view allows for analysis of the superstructure rod position. An example of a transformed image of the detector image of Au(110) in HClO$_4$ at -100 mV vs Ag/AgCl in Figure 14 can be seen in Figure 16. Here, the superstructure rods from the reconstruction can be seen as lines between the CTRs.
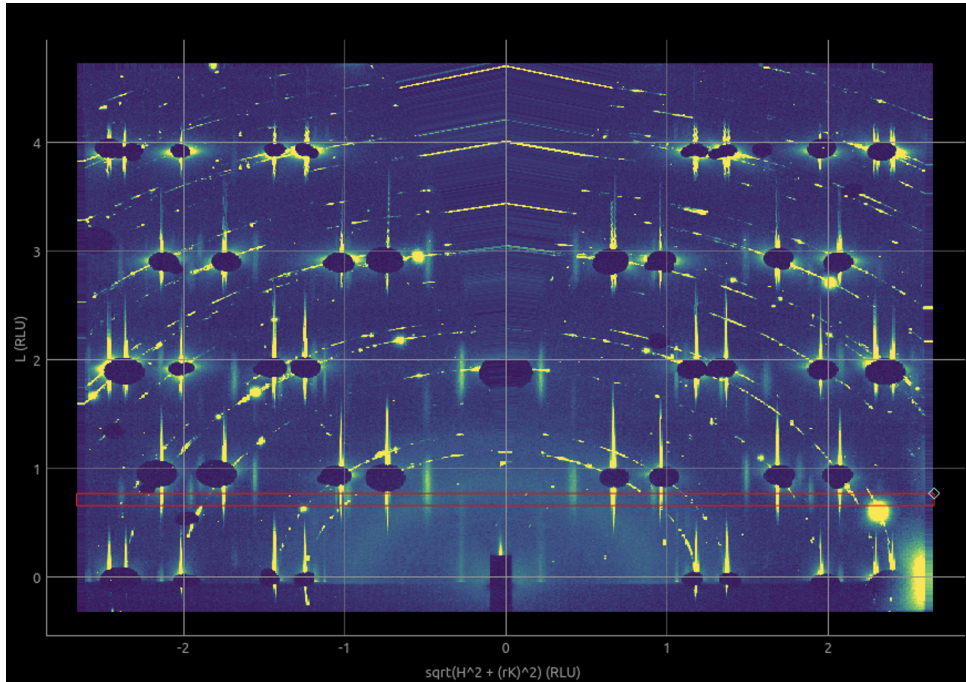


**Figure** 16: The data image of Au(110) in HClO$_4$ at -100 mV vs Ag/AgCl in Figure 14 transformed to reciprocal units. The red rectangle marks the slice in L that was used for in-plane projections below. $r = a_1/a_2$.

Using the slice in $L$ marked in Figure 16, HAT can produce an in-plane projection showing a reciprocal projection of the surface structure. An example of an unreconstructed surface can be seen in Figure 17 (Au(110) in HClO$_4$ at 600 mV vs Ag/AgCl). The $(1 \times 1)$ structure is clearly visible. Any reconstruction would be visible as signal between the substrate signal in the vertical direction (e.g., between (1,1) and (1,0) in Figure 17) since this corresponds to the $\langle 001 \rangle$ direction in real space. There will be no signal other than possible noise between the substrate spots if there is no reconstruction. The intensity within an area of interest around two substrate peaks was summed horizontally, and background was removed. The region of interest and background area of equal size can be seen in Figure 17. The relative distance of any reconstruction signal to the substrate signal will give the reconstruction order. For example, a $(1 \times 2)$ reconstruction would result in a signal at $1/2$ and $(1 \times 3)$ reconstruction a signal at $1/3$ and $2/3$.
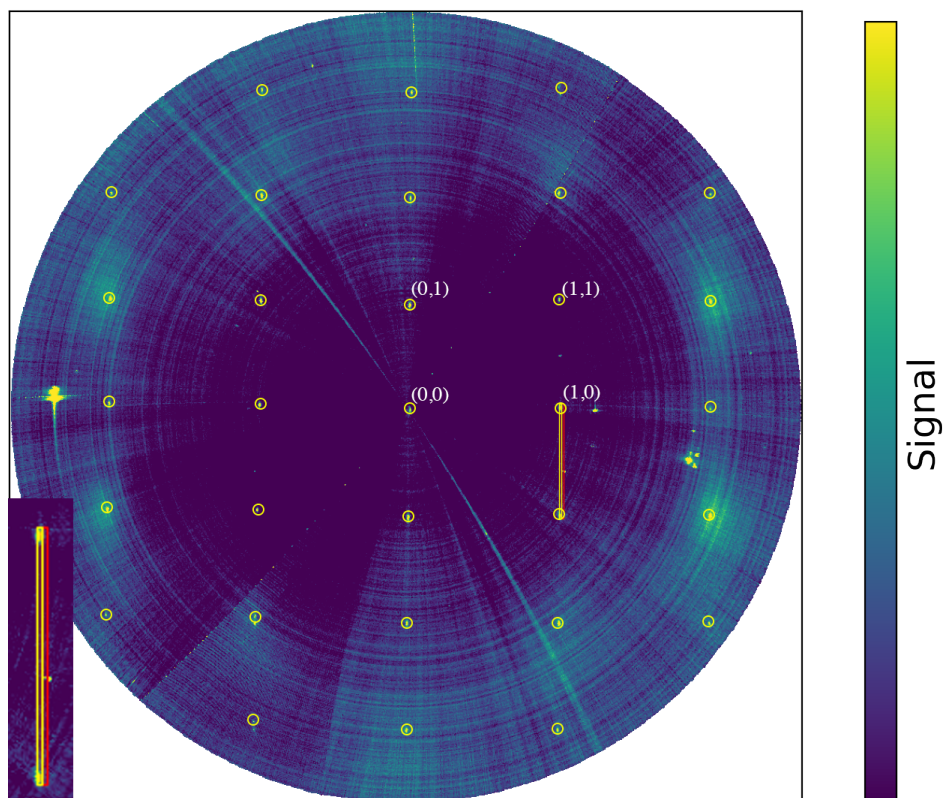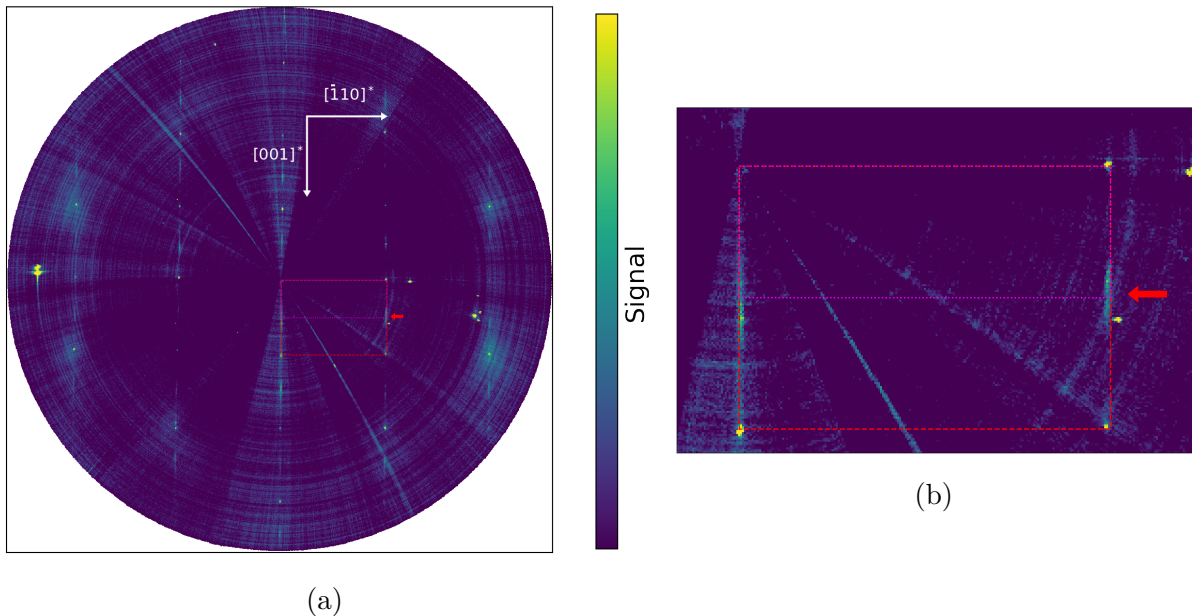
**Figure** 17: An in-plane projection of the unreconstructed Au(110) surface at 600 mV vs Ag/AgCl in $HClO_4$. The yellow circles mark the substrate lattice spots. The yellow rectangle marks the region of interest used to plot the intensity between the substrate peaks (zoomed-in at the left of the image). The red rectangle marks the area used as the background.

### 5.1.4    Data evaluation - $HClO_4$

The reciprocal space image of Au(110) at 0 mV vs Ag/AgCl in $HClO_4$ is seen in Figure 18. There are visible superstructure rods from reconstruction, but the signal is broad. The broad rods indicate small reconstruction domains since the rods will be more well defined if there are large domains of reconstruction. The broad reconstruction signal can also be seen in the in-plane projection in Figure 19 where there is reconstruction signal visible, but it is broad and weak. However, the signal is around the center between the substrate spots, indicating a $(1 \times 2)$ reconstruction.
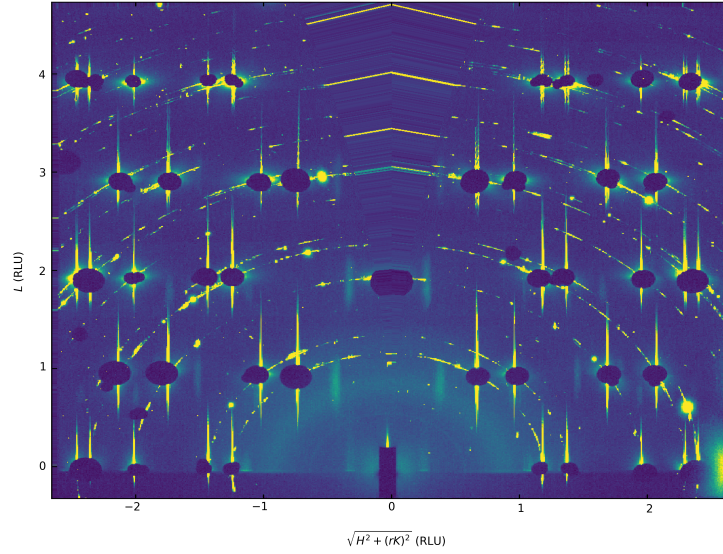
**Figure** 18: A diffraction image of Au(110) in $HClO_4$ at 0 mV vs Ag/AgCl transformed into reciprocal space units. The black areas are beam stops covering the bragg reflections. The vertical signal between the CTRs is superstructure rods.
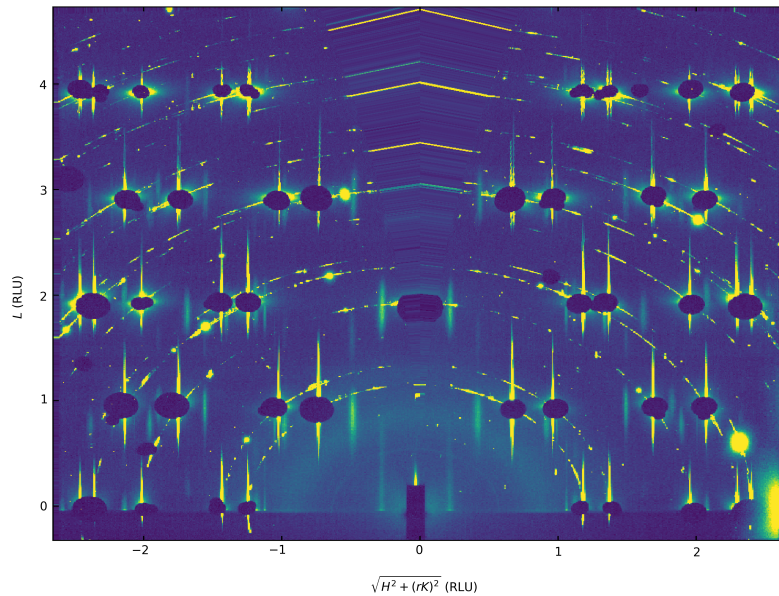


(a)

(b)

**Figure** 19: (a) An in-plane projection of the Au(110) in $HClO_4$ at 0 mV vs Ag/AgCl in Figure 18. (b) A zoomed-in image around one unit cell in (a). The red rectangle marks the unit cell of the unreconstructed surface, and the pink is the expected unit cell of the (1×2) reconstruction. The red arrow marks the center of the reconstruction visible between the substrate signal. There is only one visible reconstruction which is quite broad.

In Figure 20, the intensity of Figure 19 has been summed horizontally with a background remove using the region of interest defined in Figure 17. A Lorentzian function has been fitted to the data points and is used for qualitative analysis of the peak positions. The Lorentzian fit of the intensity in Figure 20 show that the reconstruction spot is centered at 0.49, but the intensities are weak making this number uncertain.
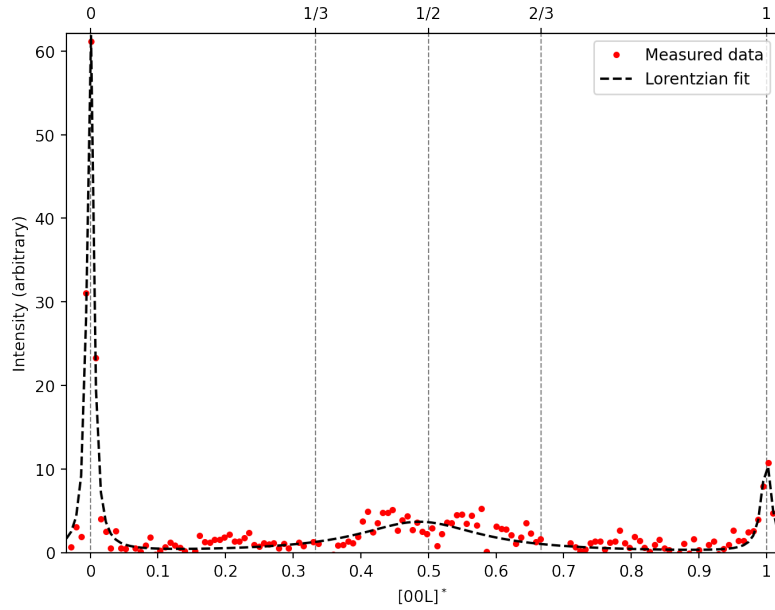
**Figure** 20: The intensity along [001]* direction from the side indicated by a arrow in Figure 19 (Au(110) in HClO$_4$ at 0 mV vs Ag/AgCl) using the region of interest shown in Figure 17. The scale is set relative to the substrate peaks. A Lorentzian function has been fitted to the peaks to find the peak center, which is at 0.49.

When a negative potential is applied, more defined superstructure rods from reconstruction is visible, which can be seen in Figure 21. In the in-plane projection in Figure 22, there are two well defined and separated reconstruction spots between the substrate signal. This would indicate a (1×3) reconstruction.



**Figure** 21: A diffraction image of Au(110) in HClO$_4$ at -100 mV vs Ag/AgCl transformed into reciprocal space units. The black areas are beam stops covering the bragg reflections. The vertical signal between the CTRs is superstructure rods.

28

(a)

(b)
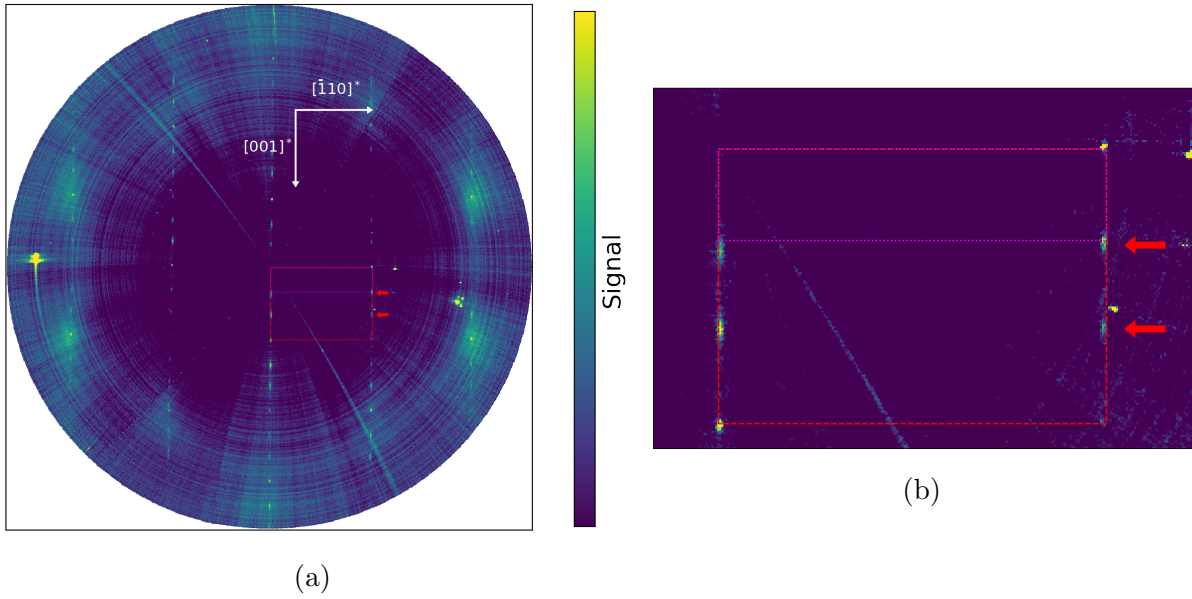
**Figure** 22: (a) An in-plane projection of Au(110) in HClO$_4$ at -100 mV vs Ag/AgCl in Figure 18. (b) A zoomed-in image around one unit cell in (a). The red rectangle marks the unit cell of the unreconstructed surface, and the pink is the expected unit cell of the (1×3) reconstruction. The red arrow marks the centers of the reconstruction signal visible between the substrate peaks. There are two clear reconstruction spots between the substrate peaks.

Figure 23 shows the summed up intensity between the substrate peaks for Au(110) in HClO$_4$ at -100 mV vs Ag/AgCl. The reconstruction peaks has their centers at 0.35 and 0.66 which strongly indicates a (1×3) reconstruction.
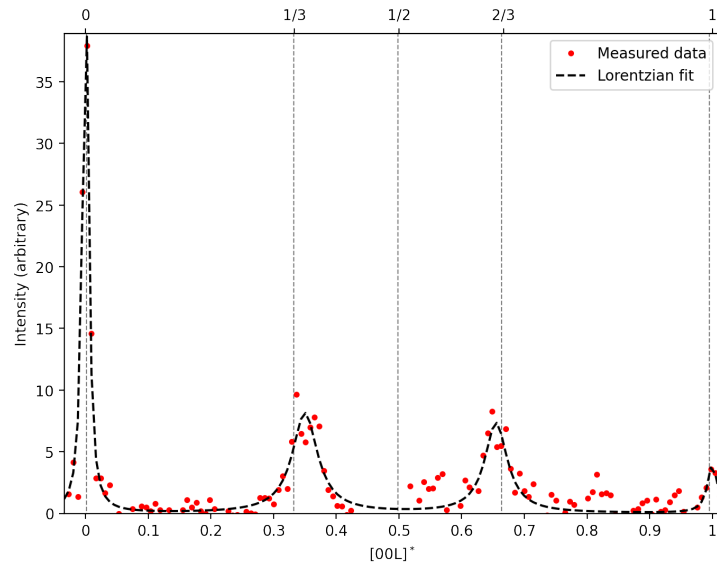


**Figure** 23: The intensity along the [001]$^*$ direction from the side indicated by a arrow in Figure 22 (Au(110) in HClO$_4$ at -100 mV vs Ag/AgCl) using the region of interest shown in Figure 17. The scale is set relative to the substrate peaks. A Lorentzian function has been fitted to the peaks to find the peak centers. The two peak centers are at 0.35 and 0.66.

In Figure 24, the plotted intensity for measurements between -100-600 mV vs Ag/AgCl can be seen. As previously discussed, there is a clear (1×3) reconstruction present at -100 mV vs Ag/AgCl. As the potential is raised, the two defined peaks disappear, and there is instead a spread-out signal centered around approximately 1/2. This broad peak narrows around 1/2 until a well-defined (1×2) reconstruction peak is visible at 400 mV vs Ag/AgCl. There is no reconstruction signal left after 400 mV vs Ag/AgCl. This indicates that the surface transitions from a (1×3) reconstruction to a (1×2) reconstruction at higher positive potentials. The transition creates small reconstruction domains and roughening, leading to the broad signal. The signal is lifted above 400 mV vs Ag/AgCl since no reconstruction is no longer stable.
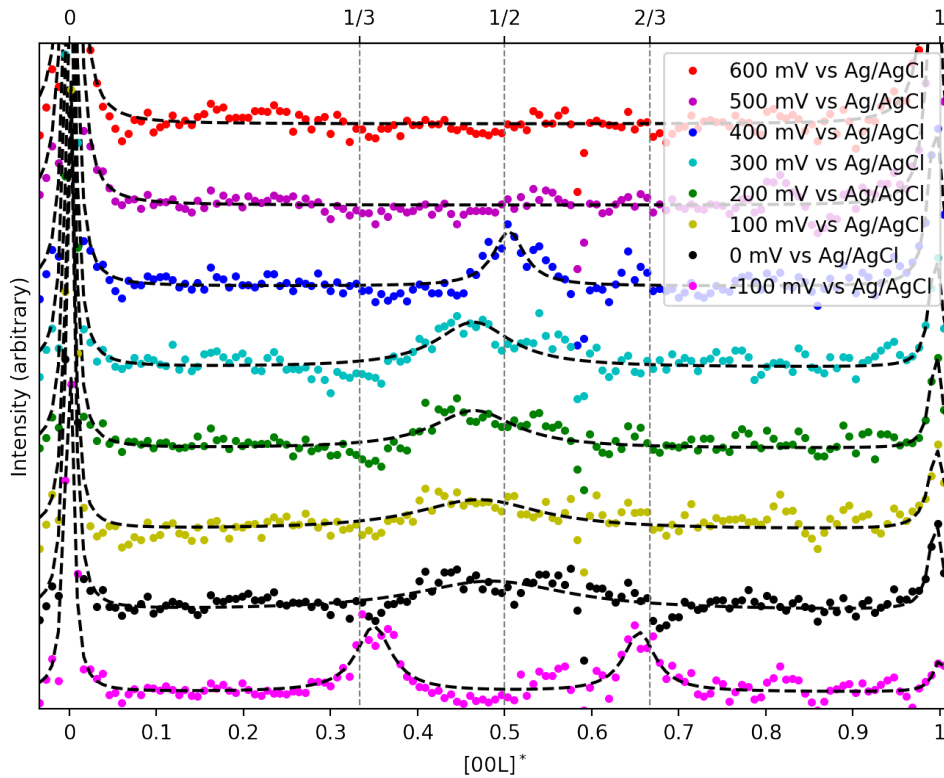


**Figure** 24: The intensity along the [001]* direction for Au(110) at potentials between -100-600 mV vs Ag/AgCl in HClO$_4$. The different potentials have been shifted upwards for clarity. The Lorentzian fits are black dashed lines. The distance on the x-axis is relative to the positions of the substrate peaks. The reconstruction is a (1×3) reconstruction at negative potentials, indicated by the two peaks. As the potential is raised, the reconstruction signal becomes broad around 1/2 before having a narrow (1×2) reconstruction peak at 400 mV vs Ag/AgCl. The reconstruction is lifted after 400 mV vs Ag/AgCl.

A time scan was performed while the potential was varied at the second beamtime. To determine the type of reconstruction, rotation scans were performed at a few potentials. A reciprocal unit image of Au(110) in HClO$_4$ at -206 mV vs Ag/AgCl can be seen in Figure 25. The reconstruction is determined to be a (1×3) reconstruction as expected from the similar measurements seen in Figure 22.
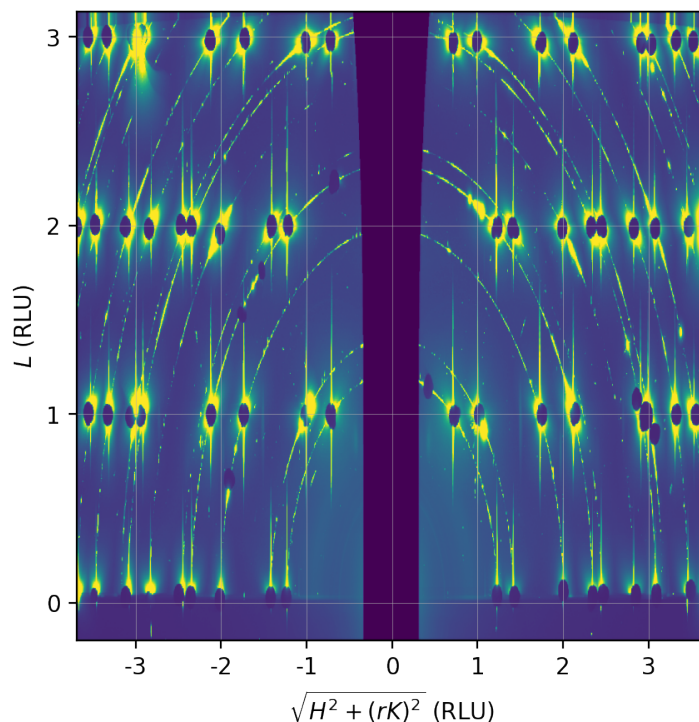
**Figure** 25: A diffraction image of Au(110) in HClO$_4$ at -206 mV vs Ag/AgCl transformed to reciprocal units. The black areas are beam stops covering the bragg reflections. The black area in the middle is the detector gap. There are weak superstructure rods of a (1×3) reconstruction.

The time scan was performed at 251° since the (1×3) superstructure rod is visible at this angle. 2100 images were captured with 0.5 s exposure time while the potential was varied. Ten images were summed up to increase the signal-to-noise ratio when analyzing. The sum of the first ten images can be seen in Figure 26. The (1×3) reconstruction determined from Figure 25 is visible, and a region of interest and background is defined to measure the reconstruction intensity over time throughout the scan.

The intensity within the region of interest and background defined in Figure 26 was summed separately for each image, and the background was subtracted. The resulting reconstruction intensity over time is plotted together with the potential in Figure 27. There is an onset of signal decrease when the potential is changed from -0.15 V vs Ag/AgCl to 0 V vs Ag/AgCl. The decrease rate lowers over time, indicating that a new stable value for 0 V vs Ag/AgCl exists. As the potential is further increased, the reconstruction signal decline more. When the signal is increased to 0.3 V vs Ag/AgCl, the reconstruction is effectively lifted. Since the sweep is performed at one set angle, the loss of this reconstruction can not be determined to be the surface returning to a (1 × 1) structure or if it is replaced with another reconstruction. However, the time scan agrees well with the set of measurements seen in Figure 24 with an initial strong (1×3) reconstruction signal that fades at low positive potential, where the signal from the first beamtime is broad. At 300 mV vs Ag/AgCl, the first set of measurements shows a clear (1×2) reconstruction signal, which is when the time scan indicates that there is no (1×3) reconstruction left.
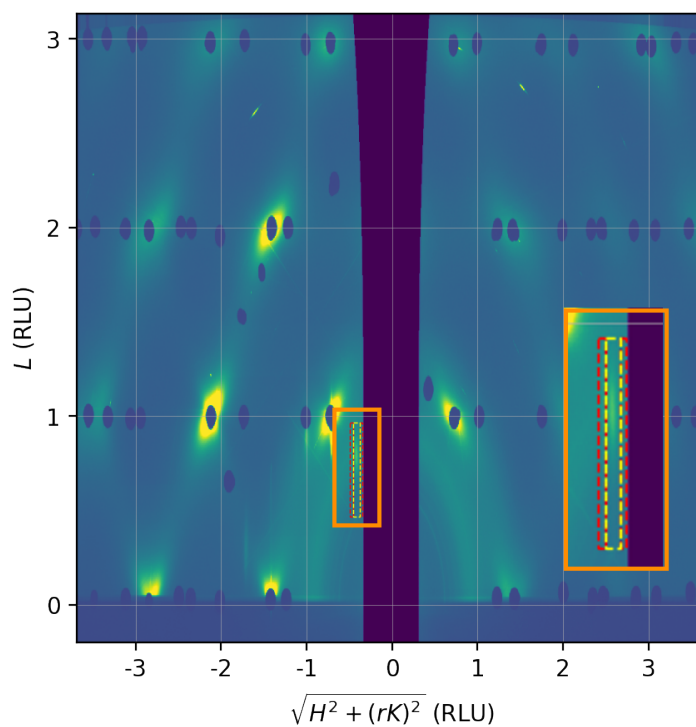
**Figure** 26: A summed-up image of the first ten images in time scan at -150 mV vs Ag/AgCl. A region of interest around a superstructure rod is marked as a yellow square, and the regions used as background are marked with a red square.
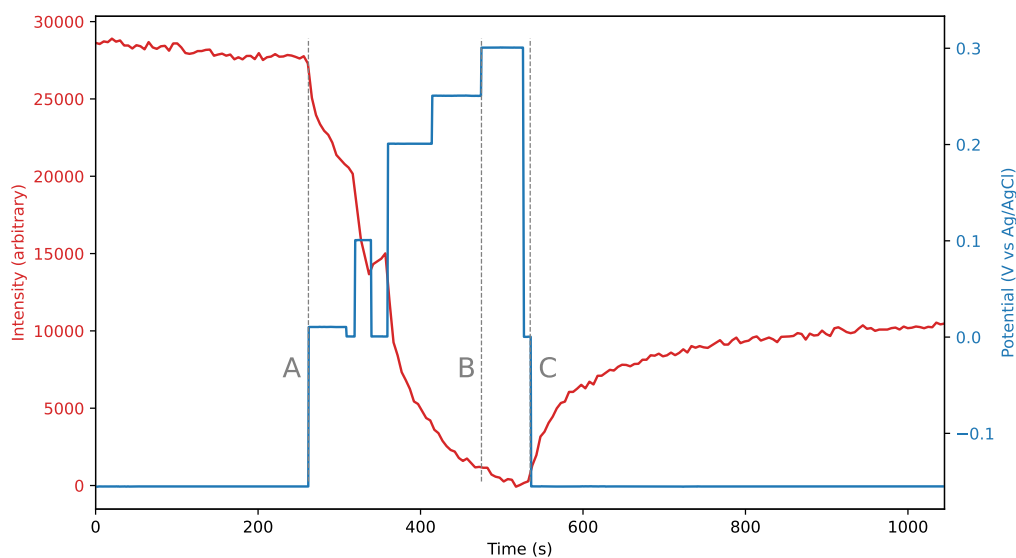


**Figure** 27: A time scan from Au(110) surface at a 251°. The intensity is the sum of the region of interest defined in Figure 26. (A) the potential is changed from -0.15 V vs Ag/AgCl to 0 V vs Ag/AgCl, and there is an immediate decrease in reconstruction intensity. The decrease is accelerated as the potential is further increased. (B) As the potential is increased to 0.3 V vs Ag/AgCl, the reconstruction is effectively gone. (C) The potential is lowered to -0.15 V vs Ag/AgCl again, and the reconstruction is slowly coming back but not to full intensity even after approximately 500 s.

When the potential in Figure 27 is lowered to -0.15 V vs Ag/AgCl again, the signal increase but to a value much lower than the initial intensity. The SOR images in Figure 28 can give a possible explanation for the loss of reconstruction signal intensity. Figure 28a is from 0 s into the time scan, and if compared to Figure 28b from 800 s, a line can be seen across the surface in the latter. This line can be damage by the x-ray beam (beam damage) that will alter the single-crystal structure.



(a)                                                                       (b)
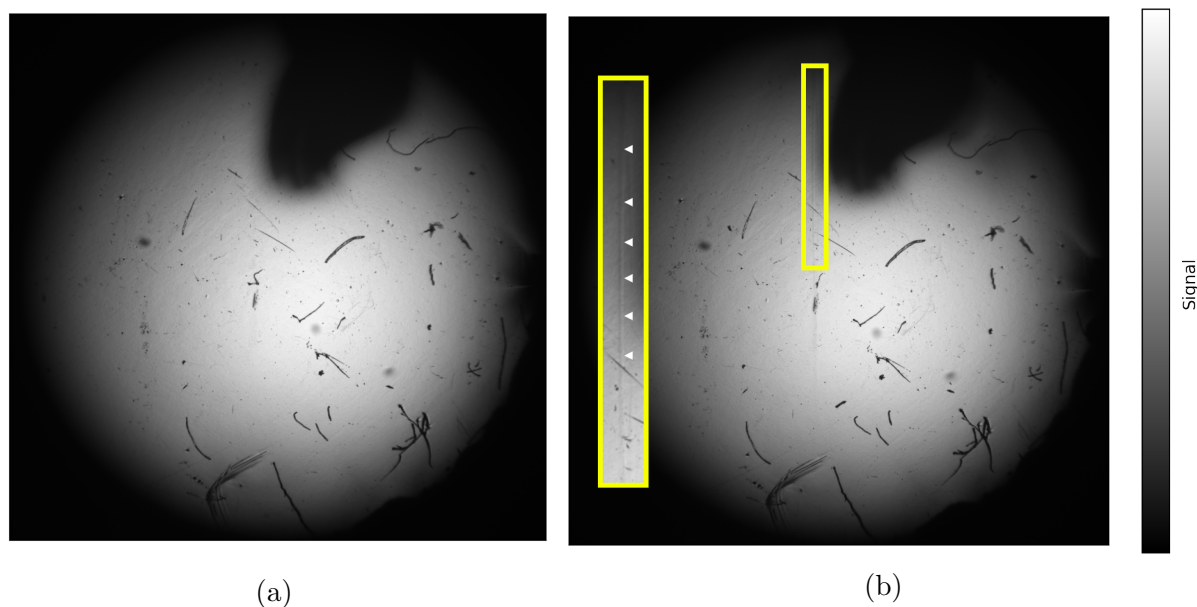
**Figure** 28: SOR image of surface during time scan shown in Figure 27 at (a) 0 s and (b) 800 s. (b) contains a zoomed-in square around visible surface change (marked with white arrows) indicating beam damage.

### 5.1.5   Data evaluation - $H_2SO_4$

The transformed reciprocal space image of Au(110) in $H_2SO_4$ at 0 mV vs Ag/AgCl can be seen in Figure 29. There is visible reconstruction signal but with a poor signal-to-noise ratio. In the in-plane map in Figure 30, the reconstruction spots are diffuse, and the noise is high, but there are two spots of reconstruction signal visible.
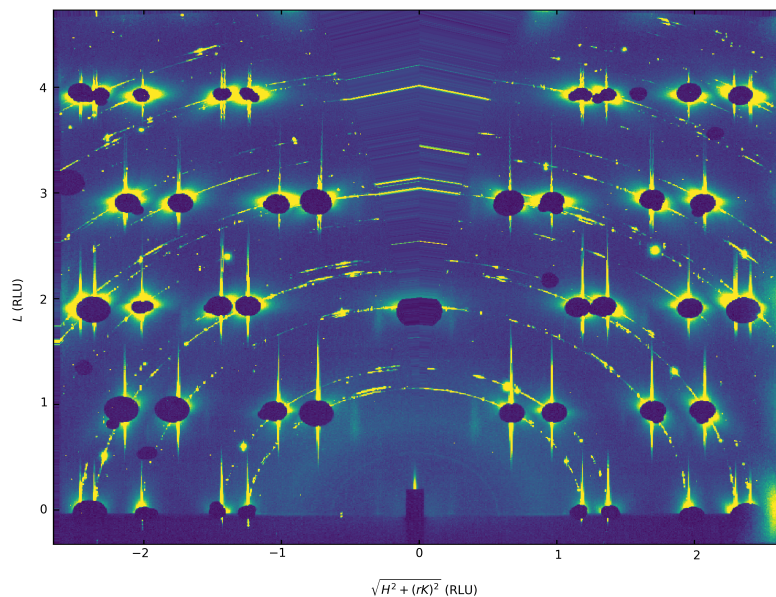
**Figure** 29: A diffraction image of Au(110) in $H_2SO_4$ at 0 mV vs Ag/AgCl transformed into reciprocal space units. The black areas are beam stops covering the bragg reflections. The vertical signal between the CTRs is superstructure rods.
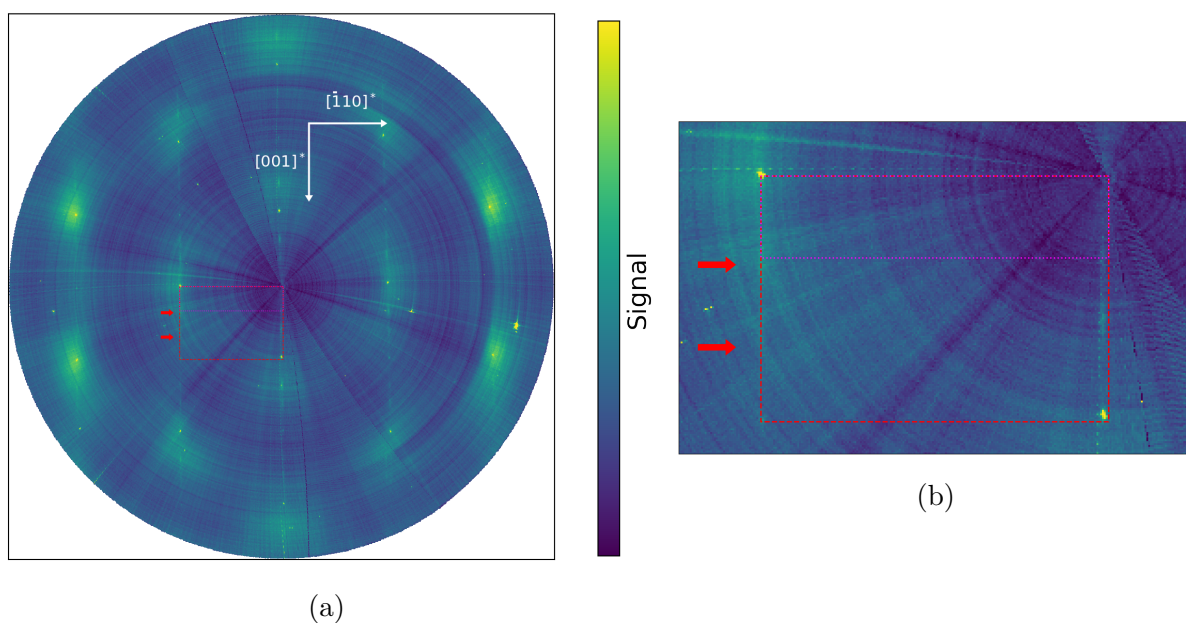


**Figure** 30: (a) An in-plane projection of the Au(110) in $H_2SO_4$ at 0 mV vs Ag/AgCl in Figure 29. (b) A zoomed-in image around one unit cell in (a). The red rectangle marks the unit cell of the unreconstructed surface and the pink the expected unit cell of the (1×3) reconstruction. The red arrow marks the center of the reconstruction signal visible between the substrate peaks. There are two diffuse spots around 1/3 and 1/6.

The intensity between the substrate peaks in reciprocal space for the Au(110) surface in $H_2SO_4$ at 0 mV vs Ag/AgCl can be seen in Figure 31. The signal peak centers are at 0.36 and 0.70 which is close to where (1×3) reconstruction would be expected.

34
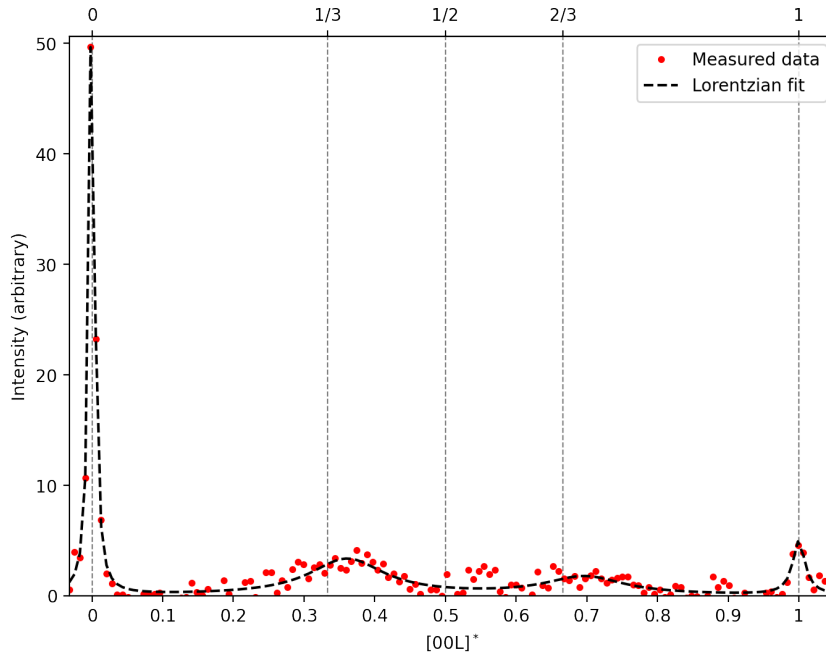
**Figure** 31: The intensity along [001]$^*$ direction from the side indicated by a arrow in Figure 30 (Au(110) in $H_2SO_4$ at 0 mV vs Ag/AgCl). The scale is set relative to the substrate peaks. A Lorentzian function has been fitted to the peaks to find the peak center. The reconstruction peaks are diffuse. The peak centers from the Lorentzian fit are at 0.36 and 0.70.

The plotted intensity for Au(110) at 0-400 mV vs Ag/AgCl in $H_2SO_4$ is shown in Figure 32. At 0 mV vs Ag/AgCl, there is some signal than can be defined as (1×3) reconstruction. A similar signal is still present at 100 mV vs Ag/AgCl. At 200 mV vs Ag/AgCl, there is a signal that is hard to place as any specific reconstruction, and no reconstruction is present at 300 mV. So the initial signal from a (1×3) reconstruction spreads out at higher potentials, but unlike the $HClO_4$, there is never a well-defined (1×2) reconstruction signal before the reconstruction is lifted at 300 mV vs Ag/AgCl.
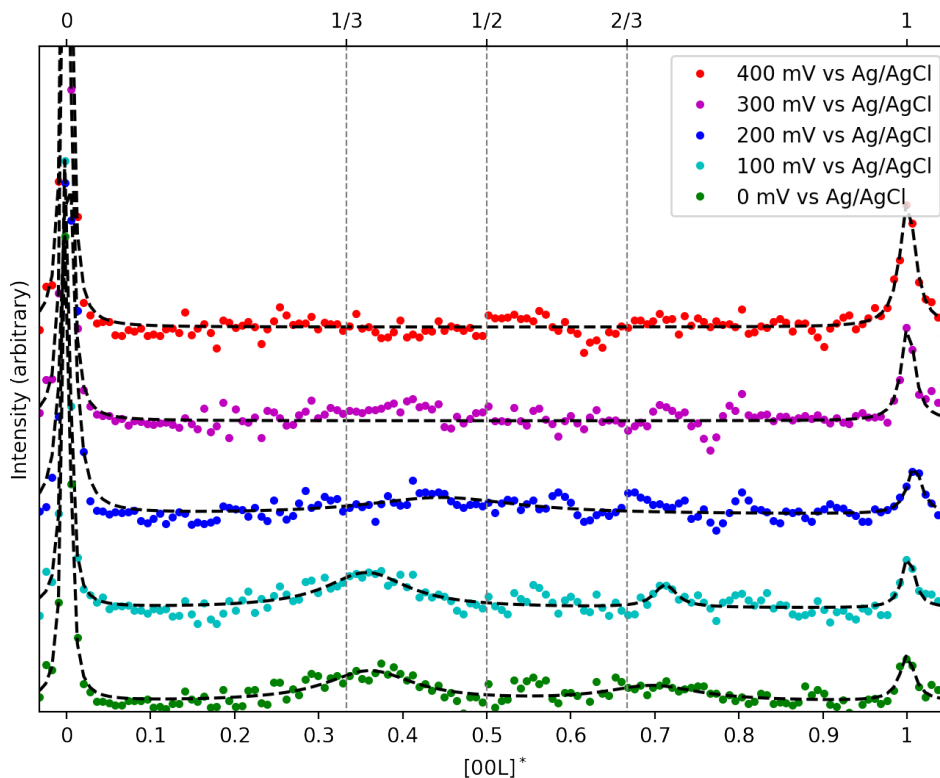
**Figure** 32: Intensity along the $[001]^*$ direction for 0-400 mV vs Ag/AgCl in $H_2SO_4$. The Lorentzian fits are dashed black lines. The distance on the x-axis is relative to the positions of the substrate peaks. At 0 mV vs Ag/AgCl, there is some signal that can be defined as $(1 \times 3)$ reconstruction. At 200 mV vs Ag/AgCl, there is a signal that is hard to place as any specific reconstruction. The reconstructed is lifted at 300 mV vs Ag/AgCl.

### 5.1.6 Discussion

For $HClO_4$, there is a transition from a $(1 \times 3)$ reconstruction at negative potentials to a $(1 \times 2)$ reconstruction at positive potentials, where the signal during the transition is broad. The time scan in Figure 27 shows that there is $(1 \times 3)$ reconstruction present during the transition, which indicates that there are simultaneous smaller domains of $(1 \times 2)$ and $(1 \times 3)$ reconstruction, which could contribute to the broader signal. Transition roughening, that previously has been observed[22], could also be a contributing factor. Before the reconstruction is lifted, there is a clear $(1 \times 2)$ reconstruction. However, no reconstruction is stable above 400 mV vs Ag/AgCl. The transition to a $(1 \times 3)$ reconstruction at lower potentials agrees with previous studies[8], and the variations in the results can be explained by environmental differences such as the concentration.

$H_2SO_4$ also indicates a similar behavior, although the $(1 \times 3)$ reconstruction is visible at a higher potential. There is indication of transition roughening, but the reconstruction seems to be less stable since it both disappears at a lower potential and a $(1 \times 2)$ reconstruction is never visible. The transition seems to occur at higher potentials for $H_2SO_4$ than for $HClO_4$, but the poor signal quality makes it hard to distinguish the reconstruction order. This and the lifting of the reconstruction at a lower potential could imply lower reconstruction stability. This difference in reconstruction behavior can stem from differences in the electrolytes but also differences in the surface preparation. The lack of defined reconstruction can not be determined not to stem from issues with surface quality.

Some transitions between reconstruction types and the transition roughening have previously been observed for both electrolytes[7, 8, 22]. Simultaneous domains are under some conditions present at Au(110) in vacuum. However, there are less defined reconstruction signals and low stability compared to the surface in vacuum conditions, which can stem from the higher disturbance from electrolyte ions adsorption. In vacuum, reconstruction may be lifted by the adsorption of a molecule, involving a charge transfer process between the molecule and the surface. In electrochemistry, this charge can instead be transferred by the potential, resulting in a lifting of the reconstruction.

## 5.2 The Electrodeposition of Sn and Pt into Porous Alumina

The method and result of creating PAA templates will first be described before the electrodeposition process. Finally, the result with different metals will be shown and analyzed.
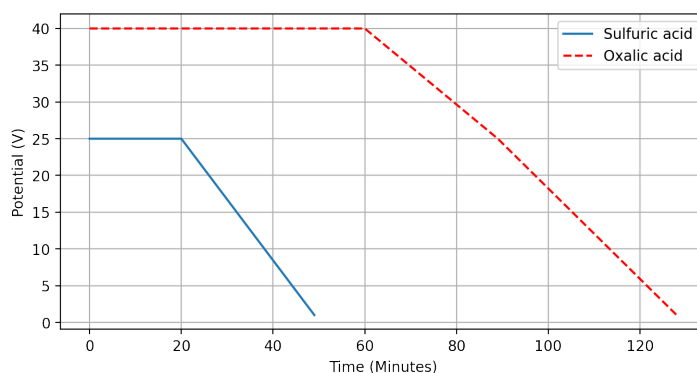
### 5.2.1 Aluminum Anodization

The aluminum sample was a 99.999 % Al foil purchased from Goodfellow. Before the first anodization, the samples were cleaned in $\geq$ 99.5 % acetone, 96 % ethanol, and ultra-pure water. The sample was placed in an electrochemical sample holder cleaned in 20 % $HNO_3$. All glass ware was cleaned in a mixture of 97 %w $H_2SO_4$ and 65 %w $HNO_3$ 1:1.

The set-up used for the anodization can be seen in Figure 33a. The CE was a Pt electrode. The electrolyte was placed in a jacketed electrochemical cell, cooled down by a recirculating refrigerated oil bath. The set-up was placed on a stirrer plate, and a stirrer was added to the electrolyte to keep an even temperature. The sample holder and CE were connected to a potentiostat and an ammeter. The current was measured throughout the anodization process.
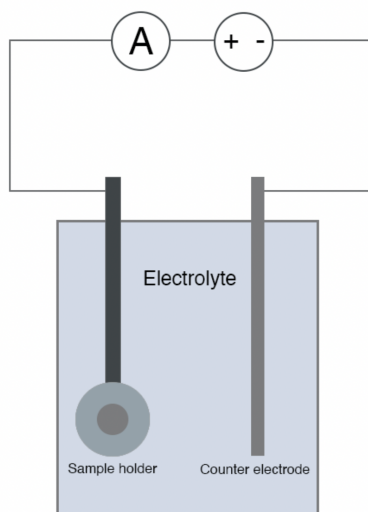


(a)



(b)

**Figure** 33: (a) The experimental set-up for the aluminum anodization with an electrolyte cooled down by a recirculating refrigerated oil bath with a stirrer, a sample holder with the aluminum surface, and the Pt CE connected to a power supply and an ammeter. (b) The potentials used for the second anodization with barrier layer thinning in sulfuric acid and oxalic acid.

The PAA templates were created using two-step anodization. The aluminum was anodized in 0.3 M sulfuric acid or 0.3 M oxalic acid. The different electrolytes will give slightly different pore properties. For the first anodization step, 0°C sulfuric acid was used, applying 25 V for 10 hours or oxalic acid with 40 V for 4 hours. The porous alumina was stripped between the anodization steps by emerging the template in a mixture of phosphoric acid and chromic acid (0.5 M $H_3PO_4$ and 0.185 M $CrO_3$) over night. The second anodization was done with either barrier layer thinning or pore widening. The barrier layer thinning was achieved by lowering the voltage, and the potentials used can

be seen in Figure 33b. For sulfuric acid, the potential was initially set to 25 V for 20 min and then lowering from 25 to 1 V for 30 min. Oxalic acid used 40 V for 1 h, then lowering to 25 V for 30 min and from 25 to 1 V for 40 min. For pore widening using $H_2SO_4$, a constant voltage of 25 V was applied for 30 minutes. The sample was then placed in 5 %w phosphoric acid at 30°C for 6 min to etch away some of the barrier layer.

An SEM image of a PAA template created in 0.3 M $H_2SO_4$ acid and barrier layer thinning can be seen in Figure 34a. The pore width is approximately 30 nm. The PAA template after anodization in 0.3 M oxalic acid and barrier layer thinning can be seen in Figure 34b. The pores are approximately 40 nm wide.



(a)                      (b)
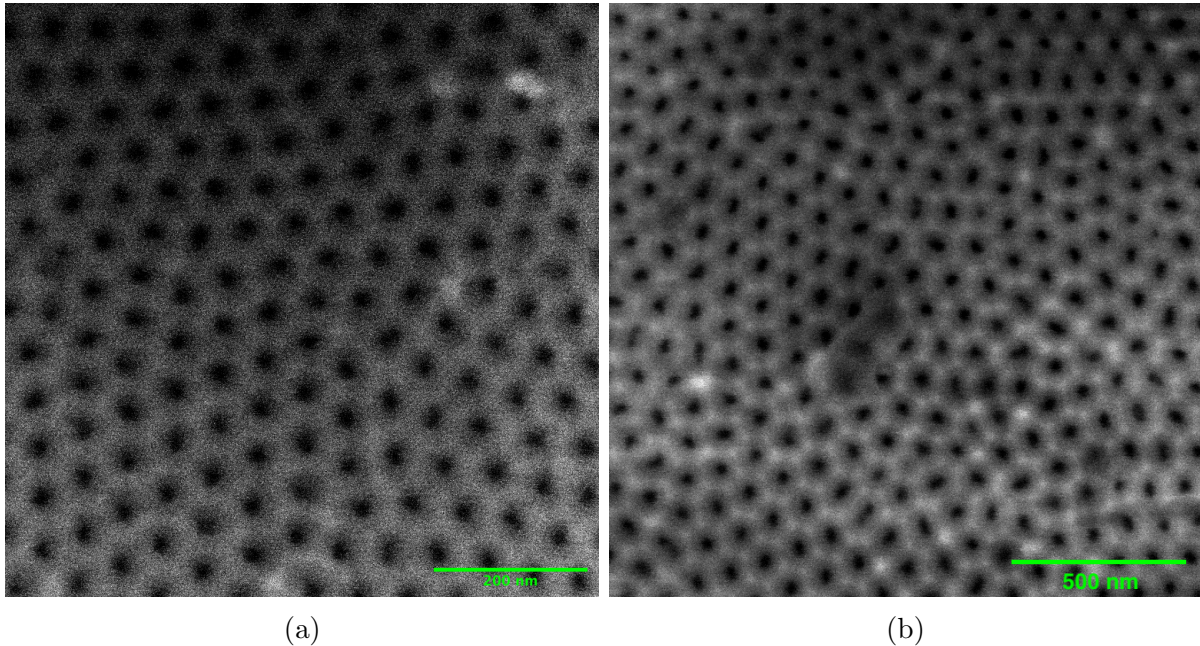
**Figure** 34: (a) SEM image of PAA template after two-step anodization in $H_2SO_4$ with barrier layer thinning. (b) SEM image of PAA template after two-step anodization in oxalic acid with barrier layer thinning. The darker spots are the pores that are organized in a hexagonal pattern.
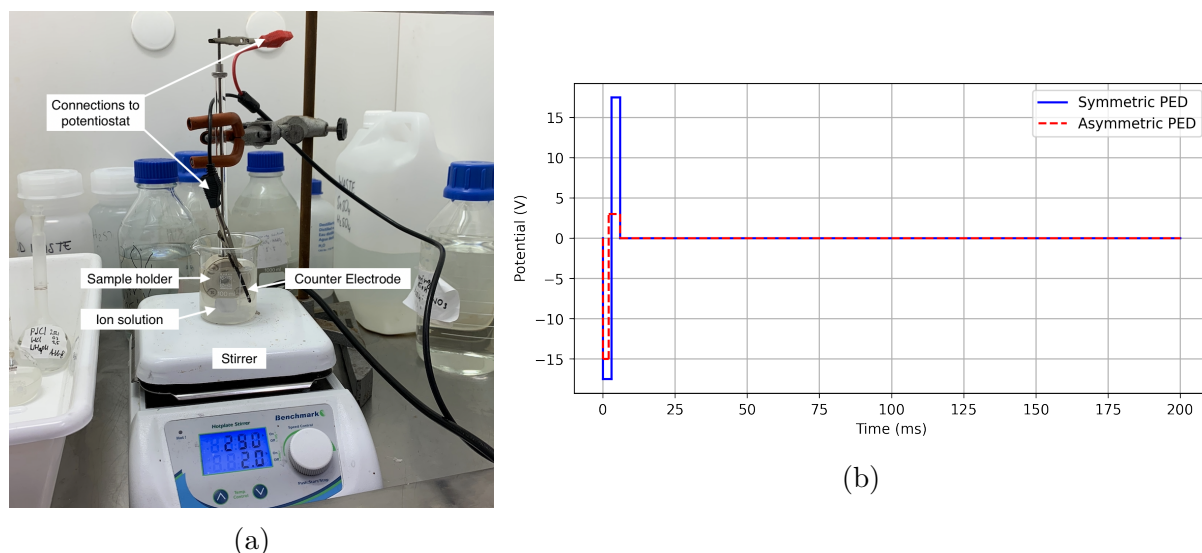
### 5.2.2 Metal electrodeposition

An image of the deposition set-up can be seen in Figure 35a. The PAA template in the sample holder was placed in the ion solution together with a clean Pt CE. The CE and the sample holder were connected to a potentiostat. The potential during the deposition was measured and recorded with a digital oscilloscope. To ensure that the solution was homogeneous, the set-up was placed on a stirrer plate.

The solution used for Sn deposition was a 0.093 M $SnSO_4$ created by first dissolving 2 g $\geq$95 % $SnSO_4$ in ultra-pure water and then adding 1.578 g 0.153 M $H_2SO_4$ and filling up with ultra-pure water to 100 ml solution. The Pt solution was a 0.03 M Platinum 5Q Plating Solution. To limit the risk of the Pt solution dissolving the PAA template due to it being acidic, the sample was thermally annealed at 350°C for 5 h before placing the sample in the solution.

Three potential shapes were used for the electrodeposition, sine deposition, PED, and asymmetrical PED. For sine deposition, a sine potential with $V_{pp} = 42.4$ V and 400 Hz

was applied. The pulse shapes for PED and asymmetrical PED can be seen in Figure 35b. Symmetric PED was done by applying a negative pulse of -17.5 V for 3 ms, followed by a positive pulse of 17.5 V for 3 ms and a rest time of 196 ms. This pulse was repeated at 5 Hz for 10-20 minutes, depending on deposition. The asymmetrical PED used a negative pulse of -15 V for 2 ms followed by a 3 V positive pulse for 4 ms and a 196 ms recovery time. The asymmetric PED was also repeated at 5 Hz for 10-20 minutes, depending on deposition.



(a)

(b)

**Figure** 35: (a) Picture of the set-up for electrodeposition. (b) The pulse shapes for PED. The symmetric PED has $V_{pp} = 35$ V and 3 ms pulse duration for both the positive and negative pulse. The asymmetrical PED has a 2 ms negative pulse of -15 V and a 4 ms positive pulse of 3 V. Both are followed by a 196 ms rest-time.
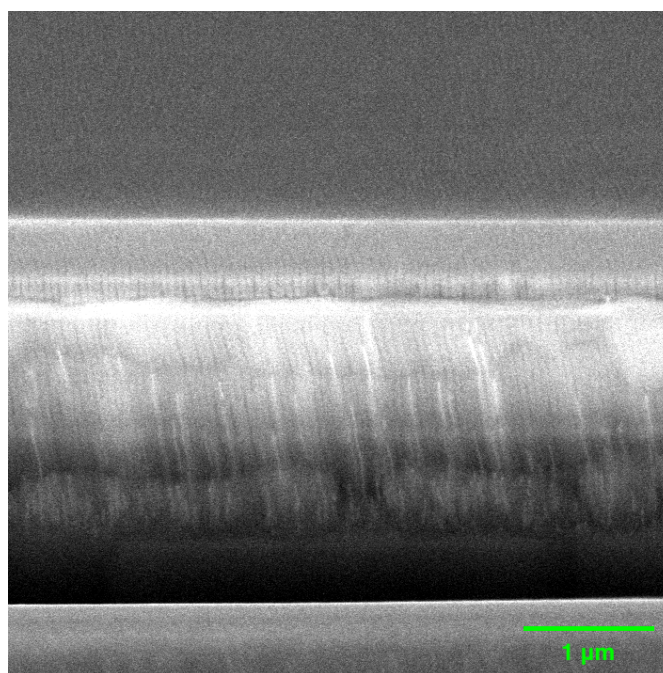
### 5.2.3   Sn deposition

The result of sine Sn electrodeposition intro a PAA template prepared in $H_2SO_4$ with barrier layer thinning can be seen in Figure 36a. The pores seem empty since no Sn is visible in the pores. However, some nano-particles of Sn might be deposited in some of the pores, causing the color change of parts of the sample that can be seen in Figure 36b. The lack of deposition can be due to the long recovery time of ions in the pores, which is a known issue with sine deposition[12, 14].

   The deposition of Sn using normal PED can be seen in Figure 37. There is material at the bottom of most pores where even branching from the barrier layer thinning is visible. Only a few pores have more material, giving wires between 0.8-1.3 $\mu$m length. The pores are approximately 1.6 $\mu$m deep. The sample has a gold color after the deposition, which can be seen in Figure 36b. The same was found even when varying the deposition time. It was also true for both deposition into sulfuric acid and oxalic acid PAA template. The hypothesis for the inability to fill the pores was the pore material dissolving during the positive part of the pulse. This would entail that the Sn would attach to the bottom of the pore but that the deposited material is then oxidized again and dissolved, resulting in poor wire buildup. The issue can also be due to re-anodization of the template during the positive part of the pulse, which would restore the barrier layer and hinder the electrodeposition.

(a)



Sine  PED  Asymmetric
PED

(b)
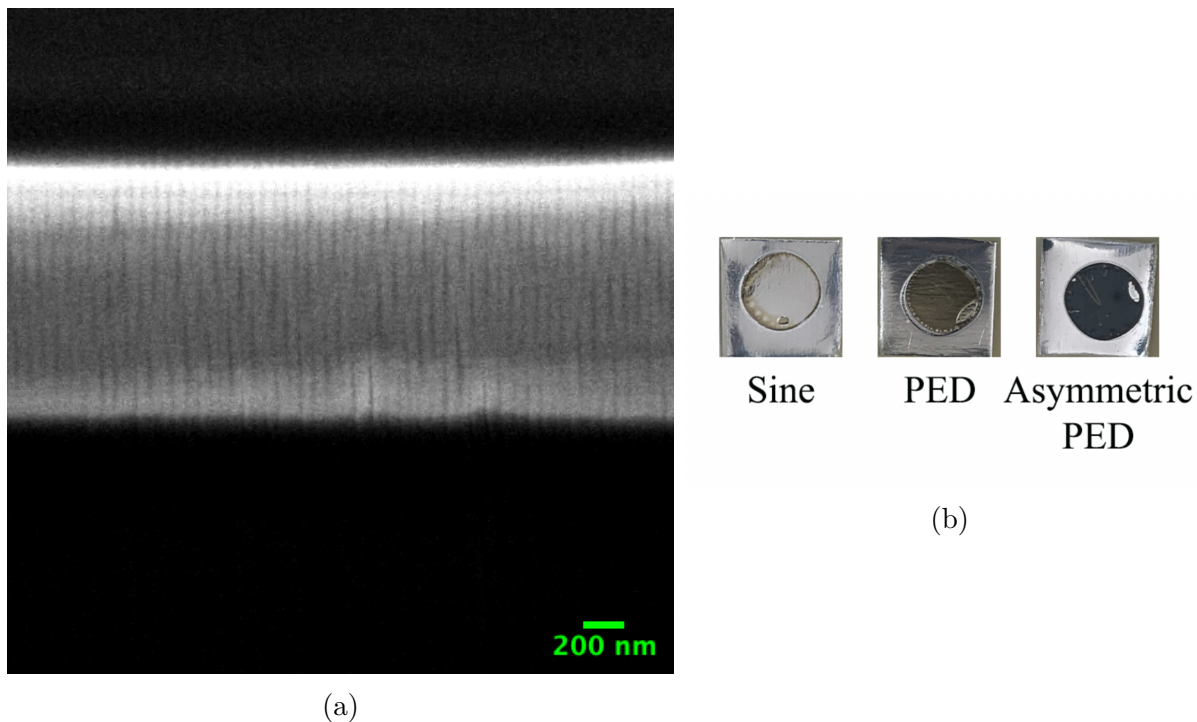
**Figure** 36: (a) An SEM image after FIB milling of Sn sine deposition into PAA template prepared in $H_2SO_4$ with barrier layer thinning. The darker vertical lines are empty pores. (b) Photos of samples that show the color change after deposition with sine deposition (left), normal PED (middle), and asymmetrical PED (right).
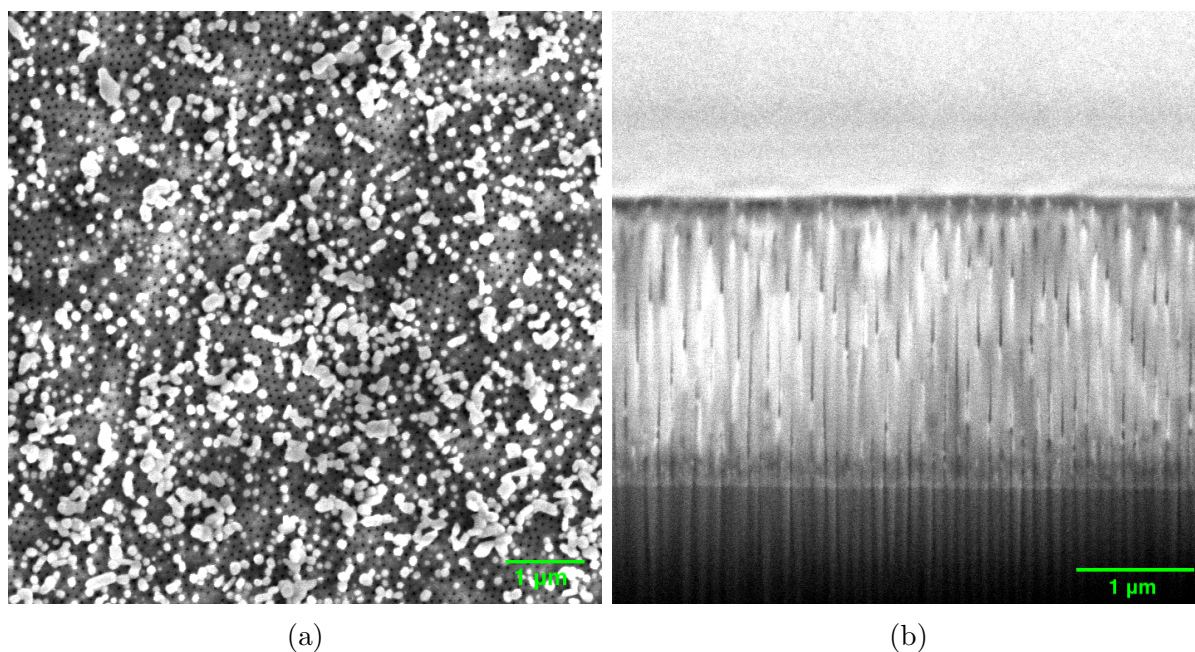


**Figure** 37: An SEM image after FIB milling of Sn deposition with PED into a PAA template prepared in $H_2SO_4$ with barrier layer thinning. The light vertical lines is the Sn wires. The light gray area above the wires is a Pt strip deposited to protect the sample wile milling.

As a solution to the issue of dissociation, the asymmetrical PED in Figure 35b was introduced. The asymmetrical PED gave a black sample which can be seen in Figure 36b. In Figure 38a, which shows a top view of the sample, it can be seen that some pores are overflown with Sn. However, this is not true for all pores. The same can be seen in the SEM image after FIB milling in Figure 38b. The wire length varies between 1 $\mu$m and the full pore length of 2.2 $\mu$m.



(a)          (b)

**Figure** 38: (a) SEM image from above of 30 min asymmetric electrodeposition of Pt into PAA template prepared with barrier layer thinning in oxalic acid. Light areas are Sn wires sticking out of pores. (b) SEM image after FIB milling of the sample in (a). The light vertical lines are Sn in the pores. The light gray area at the top is a Pt strip deposited to protect the sample while milling.

### 5.2.4  Pt deposition

Pt deposition was performed using the same electrodeposition method as for the Sn wires in Figure 38b. The asymmetric deposition into a PAA template prepared in oxalic acid with barrier layer thinning gave the result seen in Figure 39a. The wires seem to be empty. Since the sample changed color, as shown in Figure 39, there should be material in the pores. In Figure 39b, there are white spots at the bottom of the pores, which can be nanoparticles of deposited Pt. The same result was given when varying the template preparation and deposition time. The unsuccessful deposition can stem from the acidic Pt solution dissolving the Pt at a higher rate than the deposition.



|              (a)              |              (b)              |
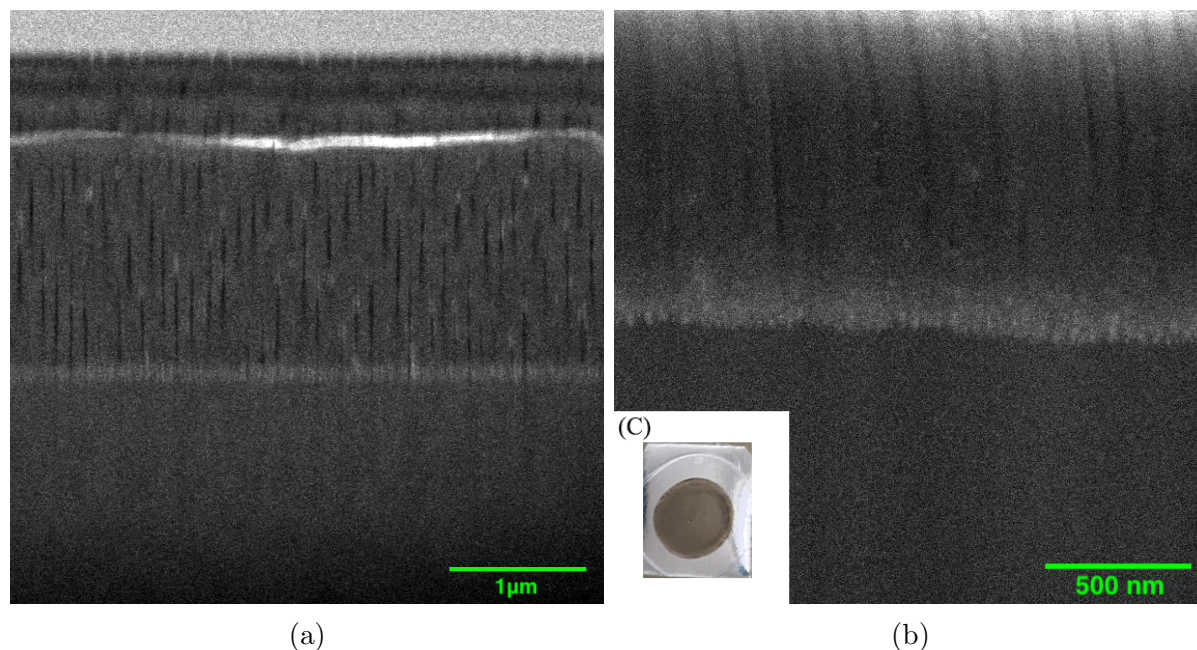
**Figure** 39: (a) SEM image of 60 min asymmetric electrodeposition of Pt into PAA template prepared with barrier layer thinning in oxalic acid. The dark vertical lines are empty pores. The light gray area at the top is a Pt strip deposited to protect the sample while milling. (b) Zoomed in picture of the bottom of the pores of the sample in (a). (c) The PAA template after asymmetrical pulsed Pt deposition.

### 5.2.5  Discussion

Using a two-step anodization process, PAA templates were created in both oxalic acid and sulfuric acid. Sn and Pt were then deposited into the templates using electrodeposition. Figure 36a and 37 show that electrodeposition of Sn was more successful using a pulsed potential shape instead of a sine potential, which is to be expected considering the mass transfer limitation of ions to the pore bottom. There was some issue limiting the amount of deposited material in the pores with the symmetrical deposition. This could either be re-oxidation of the deposited material during the positive part of the pulse or re-anodization of the template building up the barrier layer. Figure 38b shows that a better filling ratio was achieved by using the asymmetrical pulse shape shown in Figure 9 with a lower positive pulse. An asymmetrical pulsed deposition is not common, and studying this potentially more stable PED shape can be useful if more challenging materials are of interest. However, the deposition was unsuccessful for Pt, but this seems to stem from a

Pt solution issue and not the deposition method. If similar stability had been found, it could open up the possibility for parallel Pt and Sn deposition.

# 6 Conclusions

The reconstruction of Au(110) was studied in two different electrolytes at different potentials using HESXRD. For both 0.3 M HClO$_4$ and 0.3 M H$_2$SO$_4$ as the electrolyte, the missing row reconstruction was shown to be potential dependent. Both electrolytes provide similar behavior with rougher transitions from a higher-order (1×3) reconstruction towards a (1×2) reconstruction. For HClO$_4$, the transition from a clear (1×3) reconstruction to a (1×2) reconstruction is shown to still have (1×3) reconstruction present up until a clear (1×2) is observed. Further experiments are required to determine the (1×2) reconstruction behavior and if transition roughening contributes to the broad transition signal. The behavior of transitions and parallel existence of missing row reconstruction orders is consistent with the Au(110) in vacuum. For H$_2$SO$_4$ as the electrolyte, the signal from the (1×3) reconstruction is visible at higher potentials than for HClO$_4$. However, there is no stable (1×2) reconstruction, and the reconstruction is lifted at lower potentials than for HClO$_4$. It is not possible to determine if the less stable surface and a higher signal-to-noise ratio are effects of the electrolyte or issues with the single crystal surface. In general, the electrochemical environment provides a more complex environment with more adsorption, which gives less stability and more undefined signal results when compared to vacuum studies.

Well-organized PAA templates were successfully produced with both oxalic acid and sulfuric acid. Both work as a template for creating nanowires, approximately 40 nm and 30 nm wide. The two-step anodization and electrochemical barrier layer thinning make it possible to directly deposit metals into the pores using electrodeposition. A combined FIB and SEM set-up allowed for analysis of the nanowires. The electrodeposition of Sn worked with pulsed deposition while sine-shaped potentials only deposited small amounts, indicating that the rest-time of the pulsed deposition allows ions to diffuse into the pores and avoids mass transfer limitations. An asymmetric pulsed deposition worked well to achieve full pores. However, more analysis could be done to find optimal parameters for deposition. The deposition of Pt did not work well regardless of the deposition method, which is probably due to issues with the ion solutions acidity. Finding stable deposition methods for both Sn and Pt would be required to enable alloy nanowires.

# 7 Outlook

Additional time scans using HESXRD from Au(110) looking both at (1×2) and (1×3) superstructure rods would be of interest to further determine the dynamics of the structures. The HESXRD would also be interesting to perform parallel to CV to connect the surface structure to the electrochemical processes. The understanding of the missing row reconstruction transitions in connection with surface reactions can lead to a more fundamental understanding of this single crystal electrode. Combining this with analysis of other single-crystal gold electrodes and polycrystalline electrodes can further the efficiency and use of low index metal electrodes.

Concerning the electrodeposition of Pt, a first step would be to use another Pt solution to get successful deposition. When stable deposition is achieved for both metals,

simultaneous Sn and Pt deposition would be of interest to create alloy nanowires. SnPt deposition would require careful solution preparation since the deposition rate between the metals differ. Once the combined deposition is successful, it would be of interest to remove the PAA template to get freestanding wires and test the catalytic properties of the wires. Also, studies of the wires structures using, for example, XRD and transmission electron microscopy would be of interest. Additionally, further studies of the asymmetric PED would be valuable. This could both be to vary the pulse shape and study the deposition *in situ* to find optimal deposition efficiencies and to apply the shape to other metals, such as for gold deposition.

# References

[1] C. Lefrou, P. Fabry, and J-C. Poignet. *Electrochemistry*. Springer, 2009.

[2] W. Linpé, L. Rämisch, G. Abbondanza, A. Larsson, S. Pfaff, L. Jacobse, J. Zetterberg, L. Merte, A. Stierle, Z. Hegedues, U. Lienert, E. Lundgren, and G. Harlow. Revisiting Optical Reflectance from Au(111) Electrode Surfaces with Combined High-Energy Surface X-ray Diffraction. *Journal of The ElectrochemicalSociety*, 168, 2021.

[3] M. Shao. Electrocatalysis. *Springer*, 2020.

[4] T. Maiyalagan, M. Khandelwal, A. Kumar, T. A. Nguyen, and G. Yasin. Nanomaterials for electrocatalysis. *Elsevier*, 2022.

[5] P. Skołuda. Inhibition of potential-induced surface reconstruction on Au(100) electrode by the products of tyramine electro-oxidation. *Electrochimica Acta*, 56(24):8625–8629, 10 2011.

[6] X. Gao and M. J. Weaver. Electrode potential-induced reconstruction of gold (100): effect of chemisorption on nanoscale dynamics as probed by in-situ scanning tunneling microscopy. *Journal of Physical Chemistry*, 97(34):8685–8689, 2002.

[7] K. Yoshida, A. Kuzume, P. Broekmann, I. V. Pobelov, and T. Wandlowski. Reconstruction and electrochemical oxidation of Au(110) surface in 0.1 M H2SO4. *Electrochimica Acta*, 139:281–288, 9 2014.

[8] B. M. Ocko, G. Helgesen, B. Schardt, G. Wang, and A. Hamelin. Charge Induced (1 x 3) Reconstruction of the Au(110) Surface: An X-Ray Scattering Study. *Physical Review Letters*, 1992.

[9] E. C. Sowa, M. A. Van Hove, and D. L. Adams. The missing-row model for the reconstructed Pt(110)(1 × 2) surface: A leed intensity analysis showing multilayer distortions. *Surface Science*, 199(1-2):174–182, 1 1988.

[10] I. K. Robinson, E. Vlieg, and K. Kern. Structure and roughening of the Pt(110) surface. *Faraday Discussions of the Chemical Society*, 89(0):159–168, 1 1990.

[11] W. Moritz and D. Wolf. Structure determination of the reconstructed Au(110) surface. *Surface Science*, 88(2-3):L29–L34, 10 1979.

[12] W. Linpe, G. S. Harlow, J. Evertsson, U. Hejral, G. Abbondanza, F. Lenrick, S. Seifert, R. Felici, N. A. Vinogradov, and E. Lundgren. The State of Electrodeposited Sn Nanopillars within Porous Anodic Alumina from in Situ X-ray Observations. *ACS Applied Nano Materials*, 2(5), 2019.

[13] N.A. Vinogradov, G. S. Harlow, F. Carlà, J. Evertsson, L. Rullik, W. Linpé, R. Felici, and E. Lundgren. Observation of Pore Growth and Self-Organization in Anodic Alumina by Time-Resolved X-ray Scattering. *ACS Applied Nano Materials*, 1(3):1265–1271, 3 2018.

[14] A. Larsson, G. Abbondanza, W. Linpé, F. Carlà, P. Mousley, C. Hetherington, E. Lundgren, and G. S. Harlow. Electrochemical Fabrication and Characterization of Palladium Nanowires in Nanoporous Alumina Templates. *Journal of The Electrochemical Society*, 167(12):122514, 9 2020.

[15] Weronica Linpé. *Using Light to Probe Surface Electrochemical Processes*. PhD thesis, Lund University, Lund, 2021.

[16] B. Kalska-Szostko, E. Brancewicz, P. Mazalski, J. Sveklo, W. Olszewski, K. Szymanski, and A. Sidor. Electrochemical Deposition of Nanowires in Porous Alumina. *ACTA Physica Polinica A*, 115, 2009.

[17] K. Nielisch, F. Müller, A-P. Li, and U. Gösele. Uniform Nickel Deposition into Ordered Alumina Pores by Pulsed Electrodeposition. *Wiley Online Library*, 2000.

[18] Shunsuke Yagi, Kuniaki Murase, Tetsuji Hirato, and Yasuhiro Awakura. Fe-Cr alloying of iron surface by asymmetric alternating pulsed electrolysis using trivalent chromium solution. *Electrochemical and Solid-State Letters*, 9(5), 2006.

[19] P. Hofmann. Solid State Physics: An Introduction: Lund University Libraries. *Weinheim: John Wiley and Sons*, 2011.

[20] C. Kittel. Introduction to Solid State Physics. *John Wiley & Sons*, 2005.

[21] Harald Ibach and Hans Lüth. Solid-State Physics 421 Springer. *Springer*, 2009.

[22] M. Den Nijs. Competition between surface roughening and reconstruction in (110) facets of fcc crystals. *Physical Review B*, 46(16):10386, 10 1992.

[23] T. Gritsch, D. Coulman, R. J. Behm, and G. Ertl. A scanning tunneling microscopy investigation of the structure of the Pt(110) and Au(110) surfaces. *Surface Science*, 257(1-3):297–306, 11 1991.

[24] J. Evertsson, F. Bertram, F. Zhang, L. Rullik, L. R. Merte, M. Shipilin, M. Soldemo, S. Ahmadi, N. Vinogradov, F. Carlà, J. Weissenrieder, M. Göthelid, J. Pan, A. Mikkelsen, J. O. Nilsson, and E. Lundgren. The thickness of native oxides on aluminum alloys and single crystals. *Applied Surface Science*, 349:826–832, 9 2015.

[25] S. Nenov, B. Tzaneva, S. Andreev, A. Zahariev, and V. Videkov. Effect of anodization conditions on the breakdown voltage of nanoporous aluminium oxide. *2016 25th International Scientific Conference Electronics, ET 2016*, 11 2016.

[26] Y. C. Shin. *Phenomenological study of Au and Pt nanowires grown in porous alumina scaffolds*. PhD thesis, Massachusetts Institute of Technology, Massachusetts, 2011.

[27] W.J. Stepniowski and M. Salerno. Fabrication of nanowires and nanotubes by anodic alumina template-assisted electrodeposition. In W. Ahmed and N. Ali, editors, *Manufacturing Nanostructures*, chapter 12, pages 321–357. One Central Press, 2014.

[28] Harald J Wallander, Freddy E Oropeza, Benjamin Hagman, Jan Knudsen, Edvin Lundgren, and Lindsay R Merte. Oxidation of a PlatinumTin Alloy Surface during Catalytic CO Oxidation. *J. Phys. Chem. C*, 2022:11, 2022.

[29] Y. Li and B. E. Koel. Structural studies of SnPt(100) surfaces: conditions for alloy formation. *Surface Science*, 330(2):193–206, 6 1995.

[30] O. H. Seeck. X-Ray Diffraction: Modern Experimental Techniques. *Jenny Stanford Publishing*, 2 2015.

[31] P. Willmott. An Introduction to Synchrotron Radiation: Techniques and Applications. *Wiley*, 3 2019.

[32] U. Lienert, S. Gutschmidt, M. Zemmermann, R. Nowak, and W. Drube. PETRA III Extension Project Technical Design Report. 2013.

[33] U Lienert, S. Gutschmidt, T. Bäcker, Z. Hegedüs, and T. Müller. Swedish Materials Science Beamline (SMS) at PETRA III: In-line branch (P21.2)., 2019.

[34] K. C.A. Smith and C. W. Oatley. The scanning electron microscope and its fields of application. *British Journal of Applied Physics*, 6(11):391, 11 1955.

[35] S. Reyntjens and R. Puers. A review of focused ion beam applications in microsystem technology. *Institute of Physics Publishing*, 11:287–300, 2001.

[36] W. Linpé, G. S. Harlow, A. Larsson, G. Abbondanza, L. Rämisch, S. Pfaff, J. Zetterberg, J. Evertsson, and E. Lundgren. An electrochemical cell for 2-dimensional surface optical reflectance during anodization and cyclic voltammetry. *Review of Scientific Instruments*, 91(4):044101, 4 2020.

[37] J. Kieffer and D. Karkoulis. PyFAI, a versatile library for azimuthal regrouping. *Journal of Physics: Conference Series*, 425(20):202012, 3 2013.

[38] G. Harlow and S. Pfaff. HESXRD-Analysis-Toolkit: Software for the analysis of high-energy surface x-ray diffraction data, 2 2022.